



# Assessing the effects of site heterogeneity and soil properties when unmixing photosynthetic vegetation, non-photosynthetic vegetation and bare soil fractions from Landsat and MODIS data



Juan P. Guerschman <sup>a,\*</sup>, Peter F. Scarth <sup>b,d</sup>, Tim R. McVicar <sup>a,c</sup>, Luigi J. Renzullo <sup>a</sup>, Tim J. Malthus <sup>e</sup>, Jane B. Stewart <sup>f</sup>, Jasmine E. Rickards <sup>f</sup>, Rebecca Trevithick <sup>b,d</sup>

<sup>a</sup> CSIRO Land and Water Flagship, GPO Box 1666, Canberra, ACT 2601, Australia

<sup>b</sup> Joint Remote Sensing Research Program, School of Geography, Planning and Environmental Management, University of Queensland, St Lucia, QLD 4072, Australia

<sup>c</sup> Australian Research Council Centre of Excellence for Climate System Science, Sydney, Australia

<sup>d</sup> Queensland Department of Science, Information Technology, Innovation and the Arts, 41 Boggo Rd, Dutton Park, QLD 4102, Australia

<sup>e</sup> CSIRO Oceans and Atmosphere Flagship, 41 Boggo Rd, Dutton Park, QLD 4102, Australia

<sup>f</sup> Australian Bureau of Agricultural and Resource Economics and Sciences, GPO Box 858, Canberra, ACT 2601, Australia

## ARTICLE INFO

### Article history:

Received 27 September 2013

Received in revised form 15 December 2014

Accepted 29 January 2015

Available online 21 February 2015

### Keywords:

Fractional cover

MODIS

Landsat

Australia

Ground cover

Spectral unmixing

Photosynthetic vegetation

Non-photosynthetic vegetation

Soil

## ABSTRACT

Vegetation fractional cover is a key metric for monitoring land management, both in pastoral and agricultural settings. Monitoring vegetation fractional cover continuously across large areas needs good remote sensing techniques underpinned by high quality field data to calibrate and validate algorithms. Here Landsat and MODIS surface reflectance data together with 1171 field observations across Australia were used to estimate vegetation fractional cover using a linear unmixing technique. The aim was to estimate the fractions of photosynthetic and non-photosynthetic vegetation (PV and NPV, respectively) and the remaining fraction of bare soil (BS). Landsat surface reflectance was averaged over a  $3 \times 3$  pixel window representing the field area measured and also “degraded” using a  $17 \times 17$  pixel window ( $\sim 0.26 \text{ km}^2$ ) to approximate the coarser MODIS sensor's response. These two Landsat surface reflectances were used to calculate a site heterogeneity metric. Data from two MODIS-derived surface reflectance products with a pixel size of  $\sim 0.25 \text{ km}^2$  were used: (i) the 16-day nadir BRDF-Adjusted Reflectance product (MCD43A4); and (ii) the MODIS 8-day surface reflectance (MOD09A1). Log transforms and band interaction terms were added to account for non-linearities in the spectral mixing. A cross-validation step was also included to select the optimal number of singular values to avoid over-fitting. For each surface reflectance source we investigated the residuals' correlation with site heterogeneity, soil colour and soil moisture. The best model was obtained when Landsat data for a small region around each observation were used. Root mean square error (RMSE) values of 0.112, 0.162 and 0.130 for PV, NPV and BS, respectively, were obtained. As expected, degrading the Landsat data to  $\sim 0.26 \text{ km}^2$  around each site decreased model goodness of fit to RMSE of 0.119, 0.174 and 0.150, respectively, for the three fractions. Using MODIS surface reflectance data gave worse results than the “degraded” Landsat surface reflectance, with MOD09A1 performing slightly better than MCD43A4. No strong evidence of soil colour or soil moisture influence on model performance was found, suggesting that the unmixing models are insensitive to soil colour and/or that the soil moisture in the top few millimetres of soil, which influence surface reflectance in optical sensors, is decoupled from the soil moisture in the top layer (i.e., a few centimetres) as measured by passive microwave sensors or estimated by models. This study outlines an operational combined Landsat/MODIS product to benefit users with varying requirements of spatial resolution and temporal frequency and latency that could be applied to other regions in the world.

Crown Copyright © 2015 Published by Elsevier Inc. All rights reserved.

## 1. Introduction

Accurate and timely information on vegetation cover is a key data input for assessing the impacts of land management practices (Bastin

et al., 2012) and climate related impacts such as droughts (McVicar & Jupp, 1998). Vegetation cover reduces the risk of soil erosion (Bartley et al., 2006) while maximising the productivity of the landscape, and is thus a key measure of the success of land management programmes (Leys et al., 2009).

Field-based observations of vegetation cover are costly and are thus sparse in space and time, requiring observations to be extrapolated to continuously monitor changes across the landscape. The detailed spatial

\* Corresponding author at: GPO Box 1666, Acton, ACT 2601, Australia. Tel.: +61 2 6246 5880.

E-mail address: [Juan.Guerschman@csiro.au](mailto:Juan.Guerschman@csiro.au) (J.P. Guerschman).

and infrequent temporal sampling provided by field survey can be extended by using time-series remote sensing to provide a consistent record of vegetation dynamics (Guerschman et al., 2009; Okin, Clarke, & Lewis, 2013; Scarth, Roder, & Schmidt, 2010; Schmidt & Scarth, 2009). There is now little doubt amongst both researchers and land managers of the need for the extrapolative capacity of remote sensing, combined with field measurements, to form a modern rangeland monitoring system (Bastin et al., 2012).

Groundcover can be defined as the vegetation (living and dead), biological crusts and stone that is in contact with the soil surface (Stewart, Rickards, Bordas, Randall, & Thackway, 2009). In remote sensing applications the term “fractional cover” is generally used and refers to the fractions (of an area or the pixel) of photosynthetic vegetation (PV) and non-photosynthetic vegetation (NPV, including standing dry vegetation and litter) and the remaining fraction of bare soil (BS, including stones and rock). The PV fraction can be obtained from optical sensors taking advantage of the red-near infrared feature characteristic of green leaves (Tucker, 1979). Resolving how much of the landscape is covered by NPV, particularly separating dry plants/litter from soil, is more problematic (Okin, 2007). Hyperspectral sensors are able to successfully distinguish between these elements through the lignin-cellulose spectral feature between 2000 and 2200 nm (Asner & Lobell, 2000; Daughtry et al., 2006). In contrast, multispectral sensors, such as Landsat TM/ETM + or MODIS, lack the spectral resolution to identify absorption features in these wavelengths, and therefore other approaches are needed. Guerschman et al. (2009) found that the ratio of MODIS bands 7 and 6 (centred on ~2100 and 1600 nm, respectively) used in conjunction with the Normalised Difference Vegetation Index (NDVI) could resolve the fractions of PV, NPV and BS. Alternatively, Okin et al. (2013) and Okin (2007) used variations of linear spectral unmixing techniques for resolving fractional cover using MODIS data. Scarth et al. (2010) and Schmidt and Scarth (2009) also applied similar techniques to Landsat data. Table 1 summarises the studies which estimate both PV and NPV vegetation fractional cover using multispectral data.

None of the studies listed in Table 1 have specifically studied the effect of landscape heterogeneity on the relative performance of fractional cover algorithms and their relation to the sensors used. The scale issues associated with sensor resolution and the type of entities mapped have been long recognized (Dungan et al., 2002; Woodcock & Strahler, 1987). However, many studies still fail to properly address, or ignore, the difference in spatial resolution between the sensor and the field observations because they are difficult to quantify. Often field measurements collected over tens of metres have been used to calibrate and/or validate remote sensing products with a spatial resolution of a few hundred metres. Generally, high spatial resolution imagery such as Landsat, IKONOS or similar are used as an intermediate scaling step between the field measurements to the MODIS (or AVHRR) based retrievals (e.g., Liang et al., 2002; McVicar, Jupp, Reece, & Williams, 1996a; McVicar, Jupp, & Williams, 1996b). In some cases the comparison between field measurements and MODIS retrievals has been performed directly (e.g., Yebra, Chuvieco, & Riaño, 2008). If the errors associated with these scale differences are random and normally distributed the landscape spatial heterogeneity will contribute to the overall error and will not introduce bias. However this assumption is rarely tested (see for example Asrar, Myneni, & Choudhury, 1992; Garrigues, Allard, Baret, & Weiss, 2006). In this study we address these scale issues by: (i) testing the goodness of fit of models generated with imagery of different spatial resolutions; and (ii) objectively quantifying the spectral heterogeneity at each field observation (as a proxy for the spatial heterogeneity) and assessing its relationship with model goodness of fit.

Our high-level goal was to use linear unmixing to estimate fractions of PV, NPV and BS across Australia using both the Landsat and MODIS sensors. Our specific objectives were:

- 1- Compare the goodness of fit of spectral unmixing using the Landsat sensor and two MODIS-derived surface reflectance products;

- 2- Assess the scaling issues associated with using sensors with different spatial resolutions on the unmixing goodness of fit; and
- 3- Assess the effects of soil colour and soil moisture on the unmixing performance.

## 2. Materials and methods

The fundamental materials of this study involved field measurements of vegetation cover obtained from 913 locations across Australia and surface reflectance data for those sites and dates obtained from the Landsat and MODIS sensors. We quantified the spatial heterogeneity of each site using the Landsat data. We then derived endmembers and unmixed the fractional cover using the alternative sources of surface reflectance data. We compared the performance of the unmixing models and also investigated whether the residuals (i.e., the model errors) were correlated to site heterogeneity, soil colour and soil moisture. Finally, we compared the spatial patterns of Landsat and MODIS-derived fractional cover estimates and discuss the prospects of generating Landsat and MODIS operational products that are consistent and provide similar results.

### 2.1. Field measurement of fractional cover

Field measurements of fractional cover were obtained at 913 sites across Australia (Fig. 1a) (ABARES, 2013). Exactly 78 of those sites were sampled repeatedly, resulting in a total of 1171 observations (a measurement taken at a given site on a specific date). The observations were made between July 2002 and January 2013 (Fig. 1b) and were concentrated during the Southern hemisphere autumn, winter and spring (Fig. 1c).

Following Muir et al. (2011), the field measurements use a sampling procedure of three 100-metre transects intersecting at the mid-point distributed at 60 degrees intervals, to result in a star shape, where the vegetation cover in the three strata (understorey, midstorey and overstorey) is recorded. For agricultural crops sown in parallel rows, only two 100-metre transects at 45° across the sowing lines are used. Using a tape laid on the ground the observer records at every metre, using a laser pointer, the presence of green vegetation, dry vegetation or litter, cryptogam (including mosses and algae), and several types of bare ground (i.e., crust, rock, disturbed soil). If midstorey (shrubs) and/or overstorey (trees) are present, their cover is also recorded by looking up at the metre point. Total cover fractions per stratum are obtained by dividing the number of counts of a particular cover type by the total number of counts (300 or 200). When a leaf attached to a plant is recorded the operator assesses whether it is photosynthetically active based on its colour. If green it is considered as photosynthetic, if senescent or dead it is considered non-photosynthetic.

To compare the field observations of fractional cover with the satellite estimates, an exposed planar fractional cover was calculated by merging the understorey with, when present, the midstorey and overstorey layers following:

$$E_{T\_PV} = E_{U\_PV} + E_{M\_PV} + E_{O\_PV} \quad (1)$$

$$E_{T\_NPV} = E_{U\_NPV} + E_{M\_NPV} + E_{O\_NPV} \quad (2)$$

$$E_{T\_BS} = E_{U\_BS} \quad (3)$$

where  $E_{S\_x}$  refers to the exposed fraction of the stratum S (with T = total, U = understorey, M = midstorey and O = overstorey) and cover component x (with PV = Photosynthetic Vegetation, NPV = Non-Photosynthetic Vegetation and BS = Bare Soil). The exposed fractions relate to the observed fractions as:

$$E_{O\_PV} = O_{PV} \quad (4)$$

**Table 1**

Overview of studies, ordered chronologically, using multispectral imagery to specifically estimate fractions of photosynthetic vegetation, non-photosynthetic vegetation and bare soil. The table does not include studies using hyperspectral imagery only (such as [Asner and Lobell \(2000\)](#) and [Asner, Borghi, and Ojeda \(2003\)](#)).

#	Reference	Source data	Study region and area	Study period	Approach	Accuracy/validation
1	<a href="#">Asner and Heidebrecht (2002)</a>	AVIRIS and simulated ASTER, Landsat and MODIS	New Mexico, USA. Jornada LTER, ~780 km <sup>2</sup>	June 2000 (one image used)	Used a general probabilistic spectral mixture model and produced estimates of PV, NPV and BS with AVIRIS (hyperspectral) imagery. Then tested the ability of simulated ASTER, Landsat and MODIS surface reflectance data to produce similar results.	Compared estimated and measured fractional cover in two 8-ha sites.
2	<a href="#">Elmore, Asner, and Hughes (2005)</a>	MODIS (MOD09A1)	Hawaii, USA (drylands) Big Island, 10,400 km <sup>2</sup>	2000–2004, ~170 8-day composites	Used Spectral mixture analysis (SMA), selecting endmembers from the imagery assuming pure pixels.	No quantitative comparison to field data. MODIS-derived FC compared to AVIRIS-derived FC from <a href="#">Asner, Elmore, Flint Hughes, Warner, and Vitousek (2005)</a> .
3	<a href="#">Ballantine et al. (2005)</a>	MODIS (MOD09GHK)	North Africa (N of 10° N, ~8 × 10 <sup>6</sup> km <sup>2</sup> )	One cloud free image selected Nov/Dec 2000	Used Multiple-endmember Spectral Mixture Analysis (MESMA) which included several PV, NPV and bare soil endmember to produce a thematic map of landforms of North Africa.	FC estimates used for thematic map. No quantitative comparison of FC and field data.
4	<a href="#">Okin (2007)</a>	MODIS (MOD43A4)	Southwest USA. MODIS tile h10v09, ~1.44 × 10 <sup>6</sup> km <sup>2</sup>	2000–2004, ~92 16-day composites	Developed a Relative Spectral Mixture Analysis (RSMA) technique which estimates for each pixel fractions of PV, NPV and BS (and snow) relative to a reference time. Theoretical analysis.	No quantitative comparison to field data.
5	<a href="#">Gill and Phinn (2008)</a>	ASTER	NE Australia. ~36,000 km <sup>2</sup>	Field data collected in September 2006 and April 2007 with three concurrent ASTER images	Derived endmembers from the imagery based on known locations. Performed Monte-Carlo linear spectral unmixing using two endmembers (bare soil and vegetation).	Measured FC across 38 sites. RMSE = 10% for BS. Accuracy of PV and NPV fractions not reported.
6	<a href="#">Gill and Phinn (2009)</a>	ASTER	NE Australia. ~18,000 km <sup>2</sup>	Field campaign in April–May 2007, one ASTER image of 30 Apr 2007	Improved <a href="#">Gill and Phinn (2008)</a> (#5 in this table) by using three endmembers (PV, NPV and BS) instead of two. Found endmembers of PV, NPV and BS in imagery based on field-measured spectra. Use Monte-Carlo spectral mixture analysis to derive estimates of FC.	Measured FC across 12 sites. RMSE = 4% for BS. Accuracy of PV and NPV fractions not reported.
7	<a href="#">Guerschman et al. (2009)</a>	EO-1 Hyperion MODIS (MOD09GHK and MOD43A4)	Australian tropical savannas. Hyperion: ~1400 km <sup>2</sup> . MOD43A4: ~2 × 10 <sup>6</sup> km <sup>2</sup>	Hyperion: 3 images in 2005, MOD43A4: 2000–2006, ~155 16-day composites	Used EO-1 Hyperion to unmix fractional cover using the NDVI and Cellulose Absorption Index (CAI), then extended the approach to MODIS using the NDVI and the ratio of MODIS bands 7 and 6. Assessed the accuracy qualitatively using field observations and fire scar data and total cover using grass curing measurements.	Qualitative comparison to fire scars. Quantitative comparison to PV and NPV cover in 12 sites with grass curing measurements.
8	<a href="#">Scarth et al. (2010)</a>	Landsat (TM and ETM+)	Eastern Australia (parts of Qld and NSW, ~2 × 10 <sup>6</sup> km <sup>2</sup> )	Images concurrent with field measurements: 2000–2009	Spectral unmixing of Landsat data. Included several band transforms and band ratios to account for non-linearities. Calibrated method using transect-based observations. Validated results using data from one 10 km <sup>2</sup> property with five experimental grazing management trials.	Validated using 968 observations. Overall RMSE = 11.8%, r = 0.90. No statistics reported for each fraction.
9	<a href="#">Guerschman et al. (2012)</a>	MODIS (MCD43A4)	Australia ~7.7 × 10 <sup>6</sup> km <sup>2</sup>	Images concurrent with field measurements: 2000–2010	Validated the method of <a href="#">Guerschman et al. (2009)</a> (#7 in this table) with observations from Eastern Australia. Then re-calibrated method to obtain a better agreement with observations.	Used 567 observations from E Australia. Reported RMSE of 14.7%, 25% and 20.6% for PV, NPV and BS, respectively.
10	<a href="#">Okin et al. (2013)</a>	MODIS (MCD43A4)	Rain-fed cropping region of South Australia. ~150 km <sup>2</sup>	Images concurrent with field observations in Apr, Jul and Oct 2010	Compared three approaches (i.e., Spectral Mixture Analysis (SMA), multiple--endmember SMA (MESMA), and Relative SMA (RSMA)) for estimating PV, NPV and BS. Used field measurements of fractional cover obtained by Step-point method (transects) and a photographic method.	Used 27 sites. RMSE varied depending on method ranging for PV: 7–23%, NPV: 12–29% and BS: 7–22%. RSMA particularly useful for tracking temporal changes in BS although not giving absolute values.
11	Current study	Landsat (TM and ETM+); MODIS (MCD43A4 and MOD09A1)	Australia ~7.7 × 10 <sup>6</sup> km <sup>2</sup>	Images concurrent with field measurements: 2000–2013	Spectral unmixing of Landsat and two MODIS products data using same method and calibration points. Comparison between performances and assessment of effects of site heterogeneity, soil colour and soil moisture.	Used 1171 observations from Australia. Reported RMSE of ~11.2–11.9%, 16.2–17.4% and 13.0–15.0% for PV, NPV and BS, respectively.

and

$$E_{NPV} = O_{NPV}$$

$$(5) \quad E_{NPV} = M_{NPV} * [1 - (O_{PV} + O_{NPV})] \quad (7)$$

where  $O_{PV}$  and  $O_{NPV}$  are the observed fractions of PV and NPV in the overstorey (trees),

$$E_{M_{PV}} = M_{PV} * [1 - (O_{PV} + O_{NPV})]$$

$$(6) \quad E_{U_{PV}} = U_{PV} * [1 - (M_{PV} + M_{NPV}) * 1 - (O_{PV} + O_{NPV})]$$

and

where  $M_{PV}$  and  $M_{NPV}$  are the fractions of PV and NPV in the midstorey (shrubs). Finally the exposed understorey fractions are calculated as:

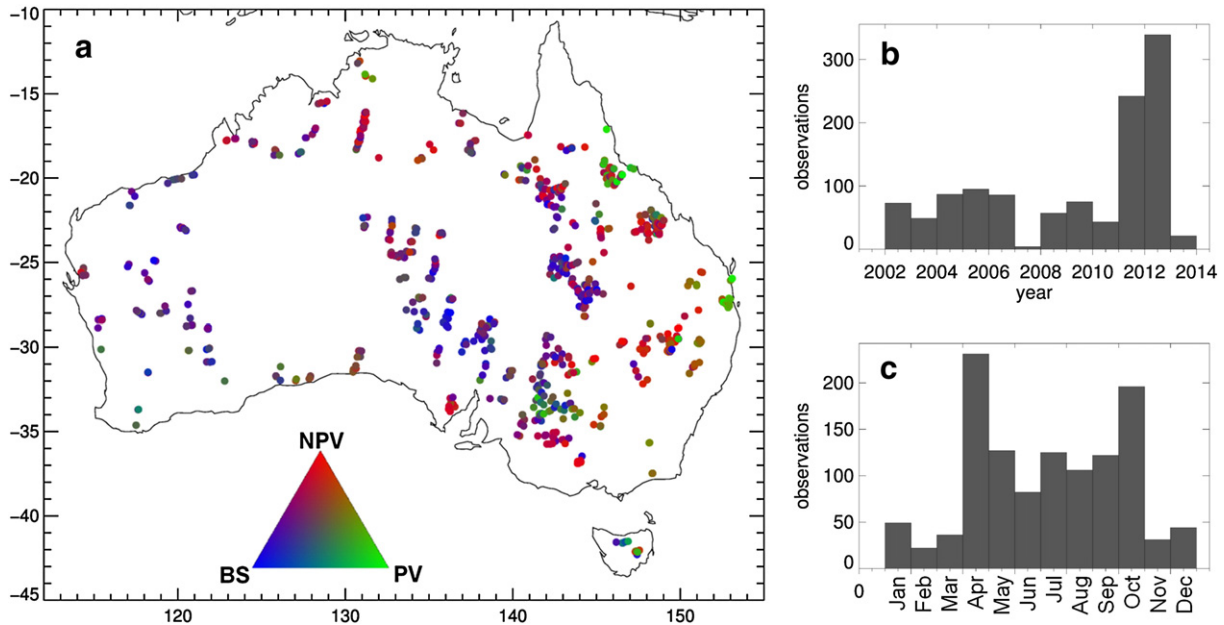


**Fig. 1.** Summary of field measurements of vegetation fractional cover. Part (a) shows the spatial distribution of field observations. Dot colours show observed fractional cover values in RGB as indicated in the legend (triangle). At sites with multiple field observations the most recent is shown; (b) number of field observations per year; and (c) distribution during the year.

$$E_{U\_NPV} = U_{NPV} * [1 - (M_{PV} + M_{NPV}) * 1 - (O_{PV} + O_{NPV})] \quad (9)$$

$$E_{U\_BS} = U_{BS} * [1 - (M_{PV} + M_{NPV}) * 1 - (O_{PV} + O_{NPV})] \quad (10)$$

where  $U_{PV}$ ,  $U_{NPV}$  and  $U_{BS}$  are the fractions of PV, NPV and BS in the understorey.

This approach assumes that the distribution of the midstorey vegetation is not affected by the clumpiness of the overstorey vegetation and similarly, the distribution of the understorey vegetation is insensitive to the overstorey and midstorey components. All the analyses that follow use the  $E_{T\_PV}$ ,  $E_{T\_NPV}$  and  $E_{T\_BS}$  fractions and are referred to as PV, NPV and BS for convenience. We assigned cryptogams to the  $E_{U\_PV}$  fraction.

The 1171 field observations span the range of possible fractional cover values (Fig. 2). The distribution of the PV and BS fractions is highly skewed to low values. There are few observations with low NPV and even combinations of PV and BS. Intuitively these distributions are sensible in the arid Australian environment as NPV cover would be expected to dominate and is usually the transitional stage between PV cover and BS, so that PV and BS will not occur without NPV present.

## 2.2. Satellite data

### 2.2.1. Landsat TM and ETM +

Data from the TM (Landsat 5) and ETM + (Landsat 7) sensors were downloaded from the United States Geological Survey (USGS) and corrected for atmosphere, topographic and bi-directional surface reflectance effects, standardised to a nadir view (i.e., satellite zenith angle is zero) and a solar zenith angle of 45° (Flood, Danaher, Gill, & Gillingham, 2013). We refer to these data herein generically as "Landsat". For each observation the Landsat image closest to the field measurement date and free of cloud and cloud shadow contamination at the vicinity of the field measurement was used, with a maximum of ± 60 days difference between the date of field measurement and the date of satellite acquisition allowed. The difference between the Landsat images and the field measurement date had a mean of −0.6 days and a standard deviation of 8.2 days (Fig. 3).

Surface reflectance for the six Landsat visible-shortwave infrared bands (i.e., not the thermal band) were obtained by averaging a 3 × 3 pixel window (i.e., a square of ~90 × 90 m) closely corresponding to the

area of the field measurement. If one or more of the nine pixels was affected by the Scan Line Corrector (SLC)-off striping effect in Landsat 7 (Markham, Storey, Williams, & Irons, 2004) then the image was not used to characterise that particular field observation. We also derived the mean surface reflectance of a 17 × 17 pixel window (i.e., an area of ~510 × 510 m) centred on the site, which we used later for quantifying the spatial heterogeneity in each observation (Section 2.2.3). Herein we refer to these two Landsat-derived surface reflectances as "Landsat 3 × 3" ( $L_3 \times 3$ ) and "Landsat 17 × 17" ( $L_{17} \times 17$ ), respectively.

### 2.2.2. MODIS

Several studies using MODIS data for deriving vegetation cover used the MODIS Nadir BRDF-Adjusted Reflectance product (MODIS NBAR) (e.g. Guerschman et al., 2009; Okin et al., 2013; Okin, 2007; see Table 1 for details). However it is not clear that the MODIS NBAR product is substantially better than the alternative MODIS 8-day surface reflectance (MOD09) series of products. Hence, we used both products to compare their relative merits when estimating vegetation fractional cover.

**2.2.2.1. MODIS 16-day nadir BRDF-Adjusted Reflectance (MCD43A4).** The MODIS 16-day nadir BRDF-Adjusted Reflectance product (MCD43A4) provides surface reflectance data as if they were taken from the nadir view and uses the solar angle calculated at local solar noon (Schaaf et al., 2002). This product uses both Terra and Aqua data from a 16-day period to provide highest quality input data. MCD43A4 collection 5 data were obtained from the Land Processes Distributed Active Archive Center (LPDAAC). These data were resampled to a geographic coordinate system using nearest neighbour resampling (Paget & King, 2008). We obtained the surface reflectance in the seven MODIS bands using the pixel which contained each site centre and in the 16-day period that included the date of each field measurement. As the MCD43A4 product is produced in a phased way with an overlap of eight days between composites we selected the field data collection date closest to the beginning of the compositing period.

**2.2.2.2. MODIS 8-day surface reflectance (MOD09A1).** The MODIS surface reflectance products from the Terra satellite (MOD09) provide an estimate of the surface spectral reflectance as it would be measured at ground level in the absence of atmospheric scattering and absorption

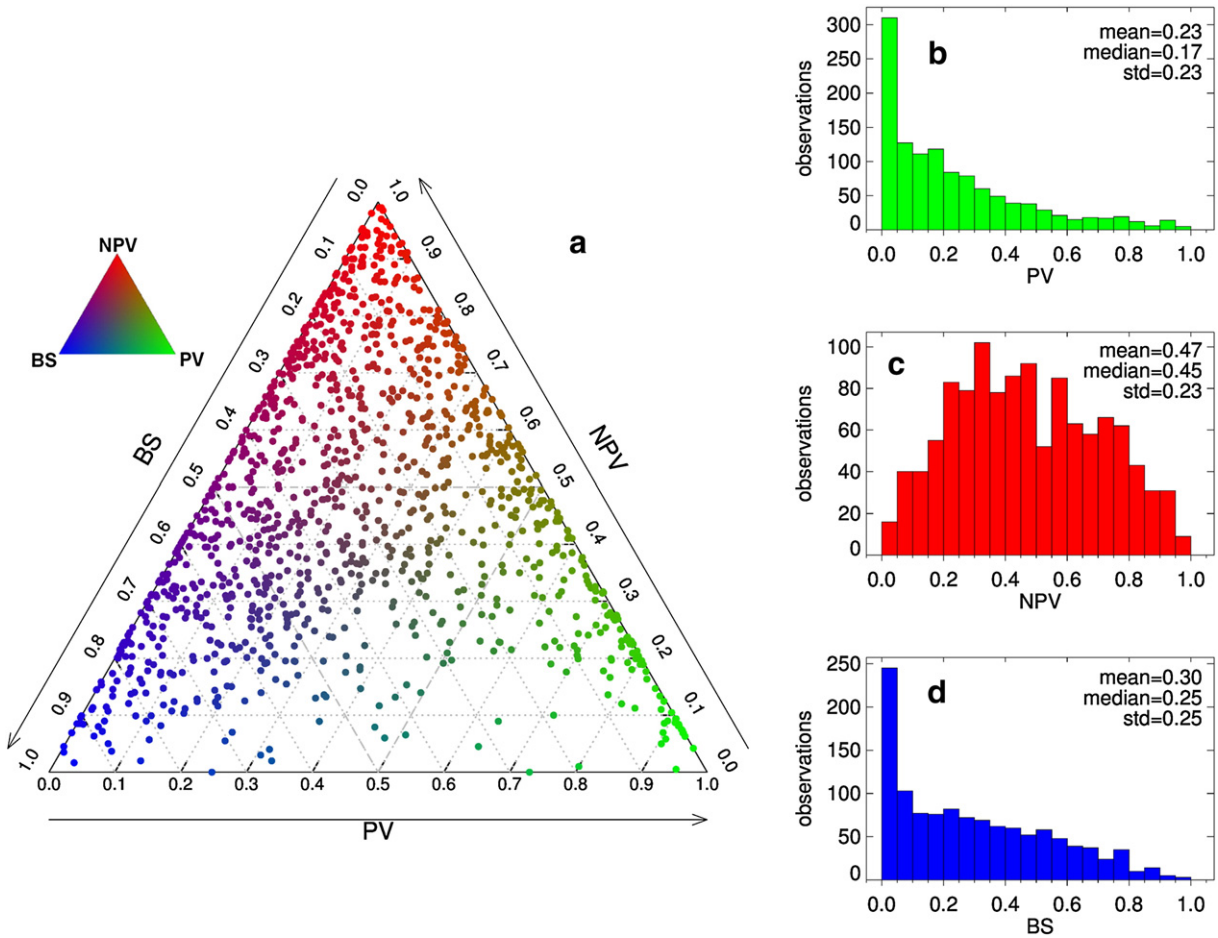


**Fig. 2.** Characterisation of field measurements of vegetation fractional cover: (a) ternary diagram showing the distribution of PV, NPV and BS fractions across the field observations. Dot colours show observed fractional cover values in RGB as indicated in the legend (triangle). Histograms of the distributions of (b) PV, (c) NPV and (d) BS are provided. In each histogram, the mean, median and standard deviation (std) are reported.

(Vermote, Kotchenova, & Ray, 2011; Vermote & Kotchenova, 2008). The 8-day composite (MOD09A1) selects the best possible observation from an 8-day window, selected on the basis of high observation coverage, low viewing angle, cloud free and low aerosol loading, with a spatial resolution of 500 m and seven spectral bands. The MOD09A1 surface reflectance data used here were subject to the same geometric processing as the MCD43A4 data.

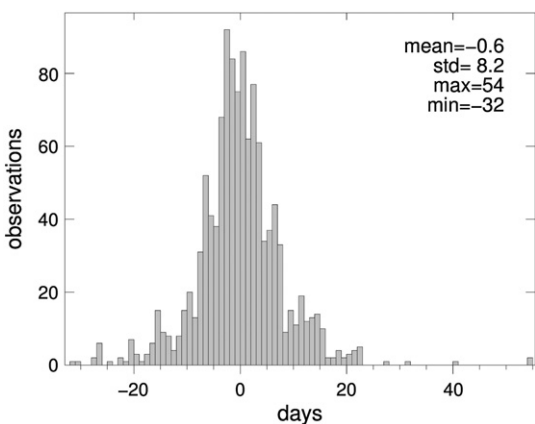


**Fig. 3.** Time difference between the acquisition of Landsat imagery and the field measurement. Negative numbers indicate that the cloud-free Landsat image was acquired before the field measurement.

### 2.2.3. Quantifying the spectral heterogeneity

We quantified the spectral heterogeneity at each field observation by comparing the surface reflectance of the area of the field measurement and the surface reflectance of a larger area around the site. For this purpose we calculated the Euclidean Distance (*ED*) between the  $L_{3 \times 3}$  and the  $L_{17 \times 17}$  surface reflectances:

$$ED = \sqrt{\sum_{i=1}^6 (L_{3 \times 3_i} - L_{17 \times 17_i})^2} \quad (11)$$

where  $i$  are the six Landsat bands. The *ED* metric is a quantification of the spectral heterogeneity in an area of  $\sim 0.26 \text{ km}^2$  (similar to a MODIS 500 m pixel) centred on the field site and is determined by the relative land cover conditions. *ED* can be interpreted as the mean difference between the surface reflectance in the  $3 \times 3$  and  $17 \times 17$  pixel windows across the six Landsat bands. The main difference of the *ED* as compared to the widely used spectral angle is that the *ED* takes into account the brightness difference between the two vectors, whereas the spectral angle is invariant with respect to brightness (Van der Meer, 2006). We expect a decrease in the goodness of fit when the  $L_{17 \times 17}$  surface reflectance is used, due to the mismatch between the spatial support of the field observation and the larger area covered by the  $L_{17 \times 17}$  reflectance. In addition, if the MODIS products had a similar ability to estimate fractional cover as Landsat, we would expect a similar goodness of fit as with the  $L_{17 \times 17}$  surface reflectance.

As the purpose of this analysis is to test the effect of sensor spatial resolution on the fractional cover estimates, we use a metric which

quantifies the change in surface reflectance with scale and assume that site heterogeneity is the main factor affecting this metric. We note that a site could still be heterogeneous but have on average a similar surface reflectance when degrading the spatial resolution (i.e., as in a checker board pattern).

### 2.3. Soil data

Soil reflectance is highly variable as a function of colour (Escadafal, Girard, & Courault, 1989; Viscarra Rossel, Bui, de Caritat, & McKenzie, 2010), moisture (Whiting, Li, & Ustin, 2004) and texture (Mouazen, Karoui, de Baerdemaeker, & Ramon, 2005). Soil colour and texture change across the landscape and are expected to vary between sites. Soil moisture also changes across the landscape but, most importantly, can change rapidly following wetting by rainfall and drying by evaporation and is highly dynamic. All these properties may affect the ability of algorithms to resolve the fractions of exposed soil, particularly when distinguishing BS from NPV (Guerschman et al., 2012; Okin, Roberts, Murray, & Okin, 2001).

The field observations described in Section 2.1 did not systematically record soil colour or soil moisture. Recent (i.e., from Jan 2010 onwards) observations include soil colour (Munsell Soil Color Charts, 1994), yet soil moisture is only subjectively measured (i.e., wet or dry). To derive these two soil properties consistently and objectively for the entire series we used information derived from other sources.

#### 2.3.1. Soil colour

Viscarra Rossel et al. (2010) used data from 4606 soil samples collected across Australia for which soil colour was determined spectroscopically from 350 to 2500 nm with a spectral resolution of 3 nm at 700 nm and 10 nm at 1400 nm and 2100 nm. For each sample, surface reflectance in the ranges 450–520 nm, 520–600 nm, and 630–690 nm corresponding to red (R), green (G), and blue (B), respectively, was averaged. Then they extrapolated the R, G and B values of the surficial soil colour across Australia by averaging 200 realisations obtained by sequential Gaussian simulations and produced a raster image at 5 km resolution which we used here to derive soil colour for each field site. Soil brightness was expressed as the sum of the R, G and B values (Post et al., 2000).

#### 2.3.2. Soil moisture

Two sources of soil moisture information were used to explore its effects on model performance. We used soil moisture data derived from the Advanced SCATerometer (ASCAT) onboard the MetOP series of European satellites. The specific ASCAT soil moisture data used were generated by the Technische Universität Wien (TUW) using the change detection algorithm of Wagner, Lemoine, and Rott (1999). The algorithm converts the measured radar backscatter signal into Surface Degree of Saturations (SDS) values ranging from 0 (driest conditions on record) to 100% (wettest conditions on record) for a given pixel. The SDS pertains to the top 1–2 cm in the soil profile given the scatterometer is a C-band (5.2 GHz) active radar. This product is resampled using nearest neighbour from the native spatial resolution (50 km) to 0.125-degree resolution (~12 km). Our data holdings of ASCAT SDS cover 2007–2012 and thus only a subset of the field observations (i.e., 421) were used. As the daily ASCAT data contains gaps in space (i.e., large areas with no retrievals for a given day) we calculated a 6-day soil moisture mean antecedent to the field observation.

We also used outputs of the Landscape model of the Australian Water Resources Assessment system (AWRA-L) (Van Dijk & Renzullo, 2011). This one dimensional land surface model simulates daily water stores and fluxes and has been shown to simulate top soil moisture reliably in space and time across Australia (Doubková, van Dijk, Sabel, Wagner, & Blöschl, 2012). AWRA-L provides information for the most of the study period (from 2000 to 2012) and without the spatial gaps characteristic of soil moisture retrievals from satellite sensors. We used outputs from version 3.0 in which the top soil layer depth varies between 5 and 18 cm. The spatial resolution of the model is 0.05° (~5 km in Australia).

For each observation the soil moisture for the top soil layer was averaged for the four days antecedent to the field observation.

### 2.4. Spectral unmixing

The approach of Scarth et al. (2010) was implemented to derive endmembers, cross-validate and unmix the surface reflectance into estimates of fractional cover for the two Landsat-derived surface reflectances (i.e.,  $L_3 \times 3$  and  $L_{17} \times 17$ ) and the two MODIS datasets (i.e., MCD43A4 and MOD09A1). This allowed us to directly compare the performance of the four alternative surface reflectance sources and attribute their differences to the spatial resolution and spectral characteristics of the sensors and derived products.

Fig. 4 provides a flowchart describing the process of setting up and inverting the data matrices (field and satellite) that form part of the unmixing method. Key elements include: (i) Truncated Singular Value Decomposition (SVD), which gives a pseudo-inverse of spectral data at

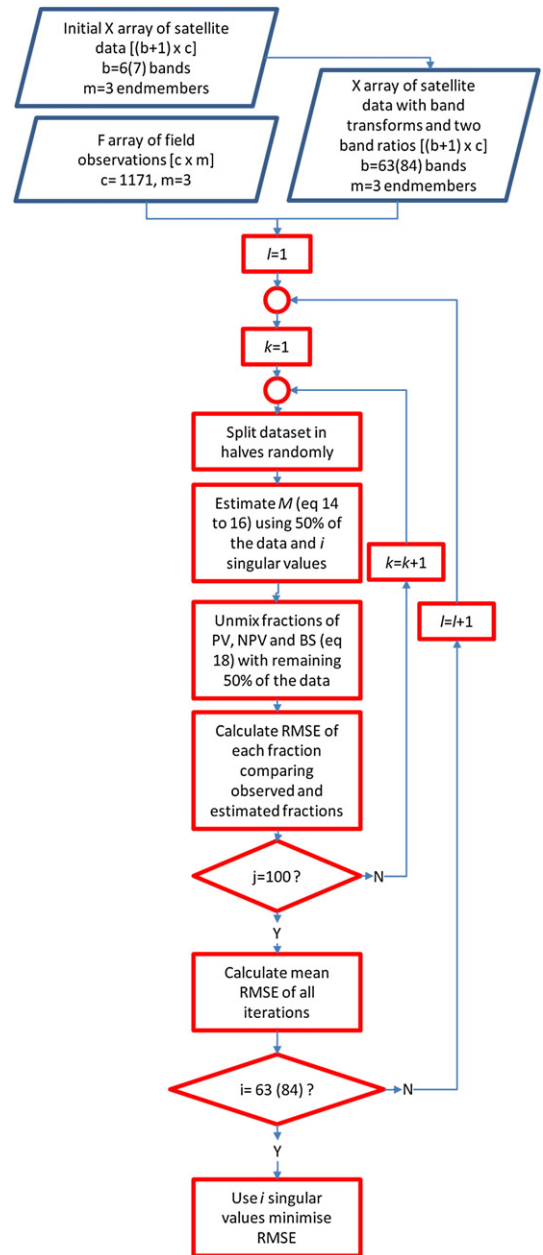


**Fig. 4.** Flowchart showing the steps taken in the inversion and cross-validation of the field and satellite data.  $k$  and  $i$  are only used as indexing values (loop counters).

each step; and (ii) cross-validation (CV) to aid in the selection of the appropriate number of singular values to avoid overfitting the model.

#### 2.4.1. Deriving endmembers

We assume a linear mixing model relationship between the multi-spectral observation and fractional cover types, i.e. a measured spectral response is a linear combination of the spectra from each cover type. The spectral endmembers for the three fractional covers (PV, NPV, BS) are unknown and derived from the data (Plaza, Hendrix, García, Martín, & Plaza, 2012). The observed spectra (obtained from the Landsat or MODIS data) for each field measurement are represented by a  $n \times b$  dimensional matrix  $X$ , where  $n$  is the number of field samples and  $b$  corresponds to the number of spectral bands. The number of endmember spectra,  $c$ , corresponds to the number of fractions of cover, in our case  $c = 3$ . The linear mixing model can be written as:

$$X = F M \quad (12)$$

where  $F$  is a  $n \times c$  matrix of fractional cover observations and  $M$  is a  $c \times b$  matrix of spectral endmembers.

This model has been used in many studies (e.g., Phinn, Stanford, Scarth, Murray, & Shyy, 2002; Scarth & Phinn, 2000). In this approach the endmembers must be linearly independent so that  $M$  is of full rank (i.e.,  $\text{rank}(M) = \max(b + 1, c)$  and invertible).

By defining an inverse operator  $A$  such that  $A M = I$  (where  $I$  is the  $b \times b$  identity matrix) we can invert Eq. (12) as:

$$F = X A. \quad (13)$$

Eq. (13) allows us to invert the field datasets and derive endmembers by regressing the satellite data against the field data and then inverting the multiple regression coefficients (see Section 2.4.2). This approach allows interactive terms to be included that assist in modelling non-linearities within the system (Dobigeon et al., 2014; Puyou-Lascassies, Flouzat, Gay, & Vignolles, 1994).

#### 2.4.2. Inverting the field observations

Using field fractional observations in the matrix  $F$  and satellite data in  $X$ , the least squares estimate of the inverse operator  $A$  is given as (Lawson, 1995):

$$A = (X^T X)^{-1} X^T F. \quad (14)$$

Truncated singular value decomposition (Xu, 1998) was used to perform the inversion in a lower-dimensional subspace. This is particularly important as we are attempting to model some of the non-linearities using variable transforms. Using  $X^+$  as the Moore-Penrose pseudoinverse (Penrose, 1955) of  $X$  we retrieve a least squares approximation to  $A$  by inverting Eq. (14) as:

$$A \approx (X^+ F). \quad (15)$$

Then we can compute the Moore-Penrose pseudoinverse of  $A$  to obtain an estimate of  $M$ :

$$M \approx A^+ \approx (X^+ F)^+. \quad (16)$$

Eq. (16) may become ill-posed if the field data does not adequately span the range of covers and their spectral variability, and relies on selecting an adequate sub-space for the inversion (Eldén, 2004). Note that this is an approach refining the widely used method which would obtain  $M$  by inverting Eq. (12) directly so that:

$$M \approx F^+ X. \quad (17)$$

We provide a demonstration of why the  $M$  array obtained by Eq. (16) differs from that obtained from Eq. (17) in the Supplementary Material and also show the implications of using one or the other on the estimated fractional cover values obtained in the unmixing. The results presented in the Supplementary Material illustrate the advantages of the refined approach used here.

#### 2.4.3. Variable transformation and cross-validation

The non-linearities in the spectral mixing were accounted for by inclusion of log transformations of the surface reflectance bands and interactive terms in the regression equations using the methods of Armston, Denham, Danaher, Scarth, and Moffiet (2009). The inclusion of interactive terms in a linear model assists in capturing non-linear influences. Specifically we added to the 6(7) bands of the Landsat (MODIS) sensors: (i) the log transform for each band; (ii) the product of all the bands with each other; (iii) the product of the log transforms of each band with each other; and (iv) the normalised ratio of all band combinations, resulting in 63 and 84 predictors (the  $b$  size of the  $X$  array) for Landsat and MODIS, respectively.

A potential issue with the inclusion of additional transforms and interactive terms in the models is that of over-fitting which may lead to poor results when used outside its calibration (Salvador & Pons, 1998). To overcome this issue we used a sub-space truncation method when calculating the pseudoinverse with the truncation value determined by the location of the lowest root mean squared error (RMSE) point using a hundred-fold cross-validation approach (Fig. 4). In each cross-validation we changed the point of the truncation by specifying the rank, and used 50% of the observations for determining the endmembers with the unmixing performed on the remaining observations. The truncated singular value decomposition method gives a low rank approximation of  $A$ , with the optimal split between the column space and nullspace being determined so that the root mean square error of the model and the observations is minimised when an independent set of observations (the validation set) is used.

#### 2.4.4. Unmixing

We introduced constraints into the fractions so that: (i)  $\sum_{i=1}^c f_i = 1$  (i.e., the fractions must sum to 100%); and (ii)  $f \geq 0$  (i.e., the fractions are non-negative). The bounded-variable least squares (BVLS), a generalisation of the non-negative least squares problem, was solved using the strategy proposed by Lawson and Hanson (1974). The BVLS algorithm was used with a weighting strategy for the sum-to-one constraint that minimises the least squared error. We modified Eq. (12) so that:

$$[X, \delta 1^n] = F[M, \delta 1^c] \quad (18)$$

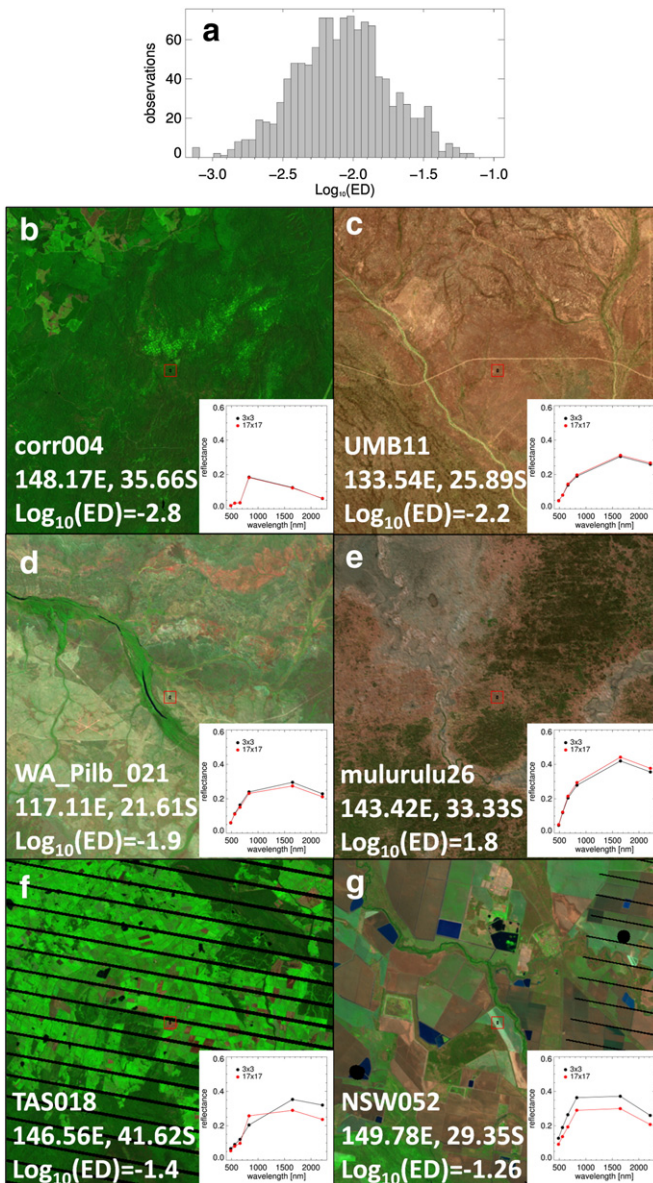
where  $\delta$  is a weighting for the sum to one constraint and  $1^n = (1, \dots, 1)^T \in R^{n \times 1}$  and  $1^c = (1, \dots, 1)^T \in R^{c \times 1}$ , i.e., they are vector of ones of dimensions  $n$  and  $c$ , respectively. The value of  $\delta$  was fixed equal to 0.2 based on Scarth et al. (2010).

### 3. Results

#### 3.1. Quantifying the spectral heterogeneity

Fig. 5 shows the distribution of the Euclidean Distance metric (ED) together with six examples of sites with different heterogeneity. The ED had a highly skewed distribution and so its logarithm (base 10,  $\log_{10}(ED)$ ) was calculated. Such a transformation has a normal distribution ( $p > 0.10$ , Kolmogorov-Smirnov test) and then statistics derived from hypothesis tests in linear models between model residuals and  $\log_{10}(ED)$  are meaningful.

We can consider a site with  $\log_{10}(ED) = -2$  (i.e., a mean difference in surface reflectance of 0.01) as relatively homogeneous (Fig. 5). Exactly 60% of the sites had a  $\log_{10}(ED) \leq -2$ . At around  $\log_{10}(ED) \geq -1.5$ , the



surface reflectance difference between a  $3 \times 3$  and a  $17 \times 17$  pixel window starts to be more marked and we could expect an important mismatch between the surface reflectance of a coarse resolution sensor like MODIS and the surface reflectance of the area actually sampled in the field.

### 3.2. Endmember generation and cross-validation

The results from the 100-fold cross validation (Fig. 4) show that for each surface reflectance source there is a particular number of singular values that provide a minimum RMSE: 24, 21, 20 and 26 for  $L_3 \times 3$ ,  $L_{17} \times 17$ , MCD43A4 and MOD09A1, respectively (Fig. 6). These numbers of singular values were used later for the spectral unmixing. However, for each surface reflectance source there was a region where the

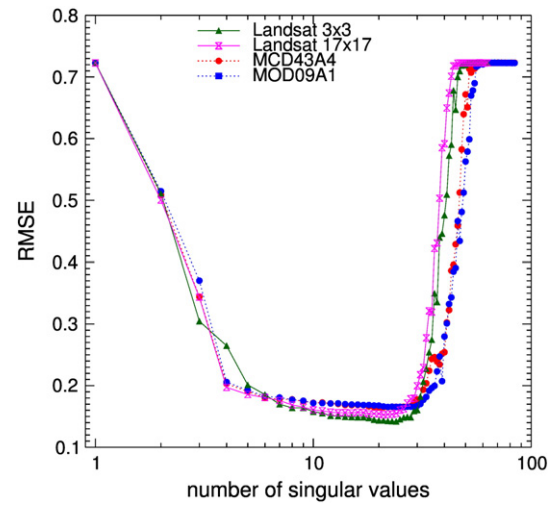


**Fig. 6.** Selection of an optimal sub-space by comparing the RMSE of the unmixing results in 100-fold cross-validation.

RMSE was close to the absolute minimum. For the two Landsat variants there was little difference in the RMSE between  $\sim 10$  and 23 singular values and for the two MODIS products such a region was between  $\sim 10$  and 34 singular values (Fig. 6).

In this paper we obtained an estimate of the endmembers array  $M$  by taking the pseudoinverse of the  $A$  array (Eq. (16)) and not by direct inversion (Eq. (17)) as is more commonly done in the spectral unmixing literature. Additionally, to account for non-linearities in the spectral mixing, we included a large number of band transforms (with an extra cross-validation step to define the optimum truncation point in the pseudoinversion of the array  $X$  to avoid over-fitting). We compare the resulting endmembers arrays  $M$  obtained with either form of inversion and with and without the inclusion of the band transforms and show the resulting fractional cover estimates in the Supplementary Material.

### 3.3. Spectral unmixing

The results from the spectral unmixing using the  $L_3 \times 3$ ,  $L_{17} \times 17$ , MCD43A4 and MOD09A1 surface reflectance data are shown in Fig. 7. Overall, the models estimate the fractional cover with a mean RMSE between 0.13 and 0.18. In all cases the models estimated PV with the lowest RMSE, followed by the BS and the NPV fractions.

Fig. 8 summarises the results of Fig. 7. As expected, the unmixing performed using Landsat ( $3 \times 3$  pixels) most closely matched the field site estimates that were collected at the same spatial support. The goodness of fit decreased when we aggregated the Landsat reflectance to a larger area, artificially generating a mismatch between the area measured in the field and the area sampled by the sensor. The unmixing of the two MODIS products (MCD43A4 and MOD09A1) had a lower goodness of fit (i.e., lower correlation and higher RMSE) to the obtained using the  $L_{17} \times 17$ . Amongst the MODIS products, MOD09A1 had a slightly better goodness of fit than MCD43A4 (Fig. 8).

### 3.4. Model residuals

To understand the effects of: (i) site heterogeneity; (ii) soil colour and; (iii) soil moisture on the performance of the unmixing algorithms presented above we investigated the correlation with model residuals. The residuals were calculated as the model estimates minus the observed values for each of the three fractions.

#### 3.4.1. Site heterogeneity

The heterogeneity of each site, measured by the logarithm of the  $ED$  between the surface reflectance in a  $3 \times 3$  pixel window and a  $17 \times 17$

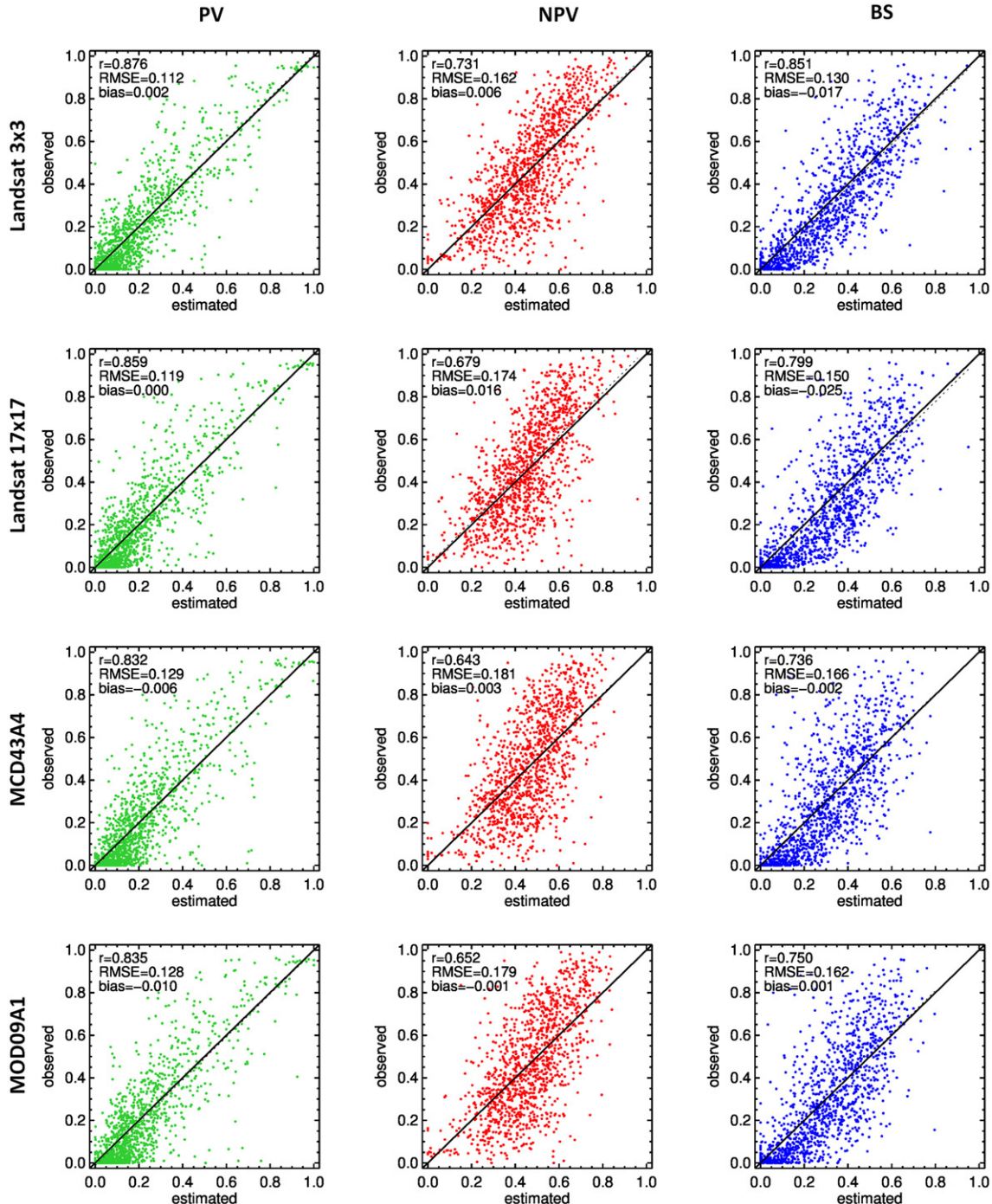


**Fig. 7.** Scatterplots showing the observed (y-axis) and estimated (x-axis) fractions of PV (left column), NPV (centre column) and BS (right column) for the Landsat 3 × 3 (top row), Landsat 17 × 17 (second row), MCD43A4 (third row) and MOD09A1 (bottom row). The black line corresponds to the 1:1 agreement, the dotted line is the linear fit between the observed and predicted values. The correlation ( $r$ ), root mean square error (RMSE) and mean bias (calculated as the mean difference between observed and predicted) are displayed.  $n = 1171$  in all cases.

pixel window (Eq. (11)) did not explain the variability in the model residuals (measured by its absolute value) of the PV fraction when Landsat 3 × 3 surface reflectance ( $L_{3 \times 3}$ ) was used (Table 2 and Figure S2). There was, however, a slight and significant ( $p < 0.05$ ) positive correlation between the NPV and BS fractions and the site heterogeneity.

When the Landsat surface reflectance was averaged over an area of  $\sim 0.26 \text{ km}^2$  around the site (i.e.,  $L_{17 \times 17}$ ) the correlation between the model residuals and the  $\log_{10}(\text{ED})$  increased, as expected. The model estimated FC on average worse in more heterogeneous sites. The results

were very similar when MODIS surface reflectance was used, either from the MCD43A4 and the MOD09A1 products.

The correlations were not very strong (the highest  $r$  is 0.23). The wide scatter in all plots in Figure S2 show that there is a large number of heterogeneous sites being estimated by the different models very accurately but also many homogeneous sites with poor model estimates.

#### 3.4.2. Soil colour

The surficial soil brightness derived from Viscarra Rossel et al. (2010) did not explain the variability in model residuals for PV and

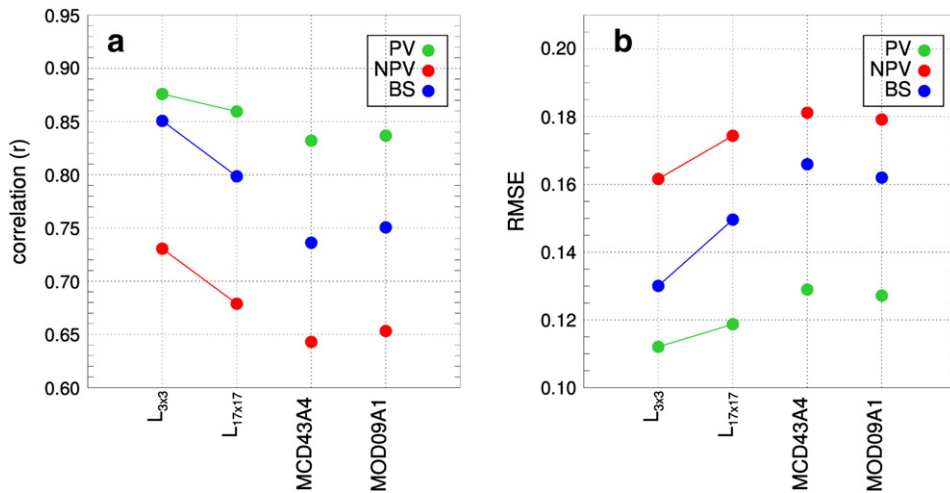


**Fig. 8.** Summary metrics for the spectral unmixing using alternative surface reflectance sources. (a) Pearson's correlation coefficient and (b) root mean square error.  $L_{3 \times 3}$  and  $L_{17 \times 17}$  correspond to the Landsat surface reflectance aggregated to alternative window sizes, MCD43A4 and MOD09A1 correspond to the two MODIS products tested.

BS, regardless of the source used for surface reflectance data (Table 2 and Figure S3). There was a small ( $r \approx 0.10$  to  $0.13$ ) and significant ( $p < 0.05$ ) positive correlation between soil brightness and the residuals of NPV.

As the vegetation (either photosynthetic or non-photosynthetic) may be obscuring the influence of soil brightness on the overall surface reflectance, we repeated the analysis only including the observations with more than 50% BS. In that case, soil brightness was negatively correlated with PV and positively correlated with BS model residuals regardless of the source of surface reflectance used (i.e., the models overestimated PV and underestimated BS for bright soils; see Table 2 and Figure S3). There was no significant

( $p < 0.05$ ) correlation between soil brightness and NPV model residuals.

### 3.4.3. Soil moisture

Soil moisture measured by the ASCAT sensor did not explain the variability in model residuals (Table 2 and Figure S4). When we used top-layer soil moisture estimated by the AWRA-L model we found similar results (Table 2 and Figure S5), i.e., a slight trend to overestimate NPV and underestimate BS in wetter conditions when  $L_{3 \times 3}$  data were used, and with very low correlation.

As in the case of soil brightness, we repeated the analyses using only those field observations with  $>50\%$  BS. Positive correlations between PV

**Table 2**

Factors affecting model goodness of fit. The table shows the Pearson's correlation coefficient ( $r$ ) and the p-value of the linear regression model fitted to the data. The models fitted were:  $y = a + bx$  where  $x$  was the residual of the fitted model for each fraction (with the exception of site heterogeneity (\*)) where  $x$  was the absolute value of the model residual). Scatterplots of the data used to generate these models are shown in the Supplementary Material (Figures S2 to S5).

	Surface reflectance source	n	PV		NPV		BS	
			r	p-Value	r	p-Value	r	p-Value
Site heterogeneity ( $\log_{10}(\text{ED})^*$ )	$L_{3 \times 3}$	1170	0.001	0.986	0.085	0.003	0.119	<0.001
	$L_{17 \times 17}$		0.053	0.069	0.152	<0.001	0.204	<0.001
	MCD43A4		0.077	0.008	0.149	<0.001	0.211	<0.001
	MOD09A1		0.080	0.006	0.173	<0.001	0.232	<0.001
Soil brightness – all sites	$L_{3 \times 3}$	1154	-0.003	0.931	0.095	0.001	-0.034	0.243
	$L_{17 \times 17}$		-0.031	0.293	0.109	<0.001	-0.033	0.262
	MCD43A4		-0.049	0.098	0.130	<0.001	-0.040	0.170
	MOD09A1		-0.048	0.105	0.113	<0.001	-0.025	0.401
Soil brightness – BS > 50%	$L_{3 \times 3}$	272	-0.113	0.062	-0.045	0.460	0.147	0.016
	$L_{17 \times 17}$		-0.208	0.001	-0.071	0.243	0.230	<0.001
	MCD43A4		-0.327	<0.001	-0.144	0.017	0.350	<0.001
	MOD09A1		-0.291	<0.001	-0.164	0.007	0.360	<0.001
Soil moisture – ASCAT – all sites	$L_{3 \times 3}$	421	0.125	0.010	0.023	0.633	-0.076	0.117
	$L_{17 \times 17}$		0.102	0.037	0.050	0.310	-0.085	0.083
	MCD43A4		0.064	0.188	-0.007	0.880	-0.003	0.949
	MOD09A1		0.053	0.281	0.001	0.983	-0.006	0.895
Soil moisture – ASCAT – BS > 50%	$L_{3 \times 3}$	93	0.255	0.014	-0.115	0.274	-0.039	0.708
	$L_{17 \times 17}$		0.281	0.006	-0.054	0.609	-0.130	0.215
	MCD43A4		0.230	0.026	0.131	0.211	-0.272	0.008
	MOD09A1		0.239	0.021	0.094	0.371	-0.239	0.021
Soil moisture – AWRA-L – all sites	$L_{3 \times 3}$	961	-0.061	0.057	0.122	<0.001	-0.064	0.046
	$L_{17 \times 17}$		-0.015	0.639	0.120	<0.001	-0.102	0.002
	MCD43A4		0.006	0.857	0.038	0.238	-0.027	0.408
	MOD09A1		-0.009	0.783	0.056	0.083	-0.032	0.316
Soil moisture – AWRA-L – BS > 50%	$L_{3 \times 3}$	212	0.012	0.861	0.102	0.138	-0.125	0.070
	$L_{17 \times 17}$		0.125	0.070	0.159	0.021	-0.242	<0.001
	MCD43A4		0.322	<0.001	0.134	0.052	-0.294	<0.001
	MOD09A1		0.274	<0.001	0.201	0.003	-0.328	<0.001

and negative correlations between BS model residuals and soil moisture were found, for all surface reflectance sources and for both ASCAT and AWRA-L-derived soil moisture (Table 2 and Figure S5). These results show a tendency to overestimate PV and underestimate BS in wet top-soil conditions, respectively.

### 3.5. Spatial patterns of fractions unmixed by Landsat and MODIS

The results provided in the sections above indicated that the differences between Landsat and MODIS seem to be largely associated with their respective spatial resolutions. This suggests that, in principle, a

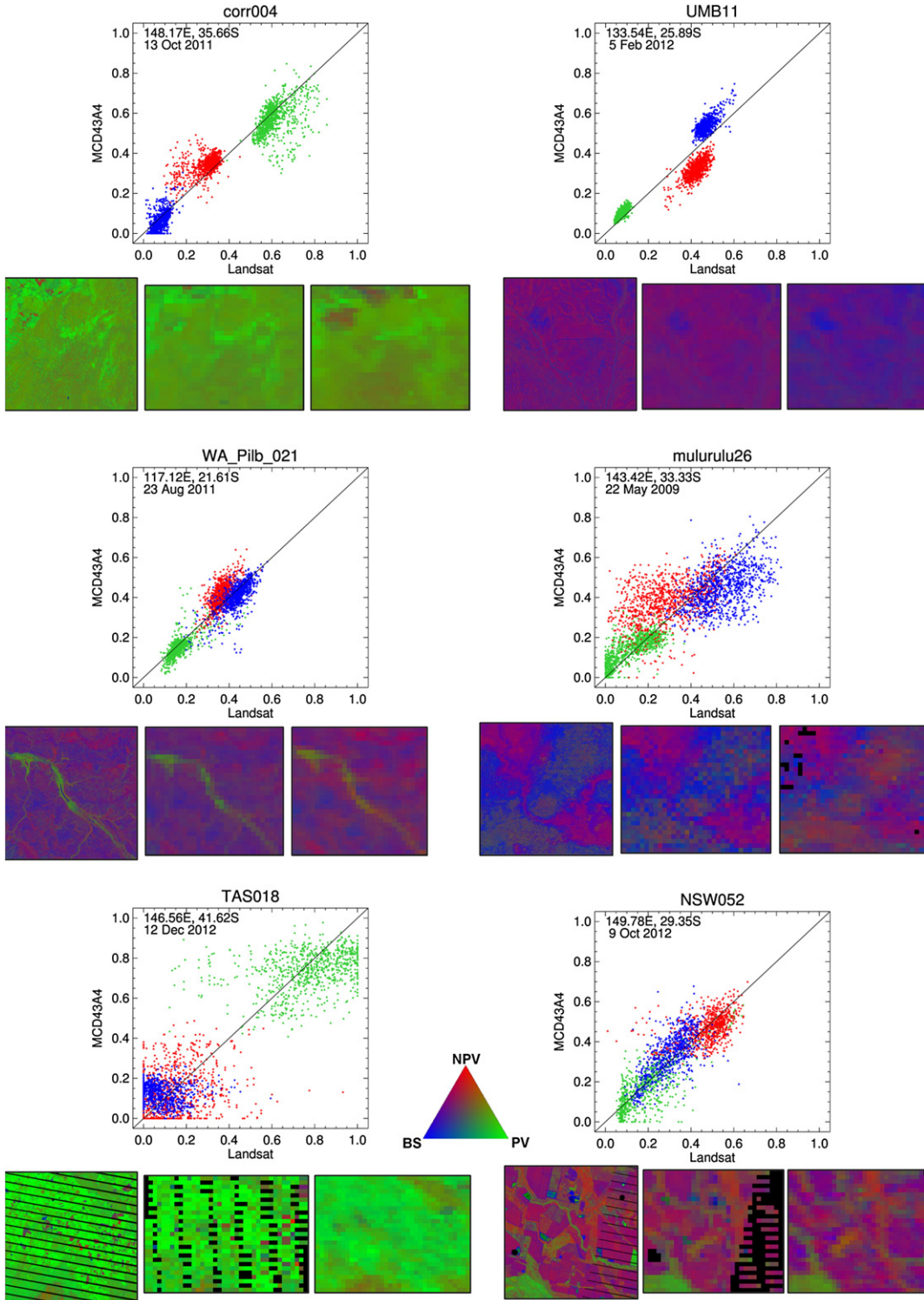


**Fig. 9.** Comparison between the unmixing results using Landsat ( $L_3 \times 3$ ) and MODIS (MCD43A4) imagery for the same six example areas shown in Fig. 5. The scatterplots show the relationship between Landsat and MCD43A4 estimates for PV (green), NPV (red) and BS (blue); the text in the top left of each scatterplot indicates the geographic location of the scene centre and the date of the field observation. The maps under the plots show the spatial patterns of the fractional cover estimates from Landsat (left), the same aggregated and reprojected to MODIS resolution (centre) and from MCD43A4 (right) for  $225 \text{ km}^2$  centred around the site. In the images PV, NPV and BS are shown in green, red and blue, respectively, as shown in the triangular legend. The black pixels in the TAS018 and NSW052 sites correspond to SLC-off areas and were ignored in the comparisons.

Landsat-based fractional cover aggregated to the MODIS resolution should give similar results to a MODIS-based fractional cover. To test this we compared the results of the unmixing performed with  $L_3 \times 3$  data and with MCD43A4. We used the original Landsat for the six examples shown in Fig. 5 which encompass varying degrees of landscape fragmentation and fractional cover conditions. These are Landsat subsets of  $500 \times 500$  pixels ( $\sim 225 \text{ km}^2$ ), and correspond approximately to a  $30 \times 30$  MODIS (500 m) pixel window (i.e., a total of  $\sim 900$  pixels). The unmixed Landsat images were aggregated and resampled to match the pixel size and geographic coordinate system of the MCD43A4 product.

Generally there was a good agreement between the Landsat and the MCD43A4 estimates of fractional cover, once Landsat was aggregated to the same spatial resolution and geographic coordinate system as MODIS (Fig. 9). There was significant amount of scatter at two sites: (i) TAS018, a highly fragmented agricultural landscape, measured during the crop growing season; and (ii) Mululuru26, an open woodland in southwest NSW, measured during a dry period. The scatter between Landsat and MODIS does not appear to be, however, directly related to the degree of landscape fragmentation as, for example, the site NSW052 is highly fragmented yet the Landsat and MODIS unmixing gave similar results. Other factors, including the spectral and radiometric properties of the Landsat and MODIS sensors, the atmospheric and BRDF corrections performed for each of them and the 16-day compositing period of MCD43A4 may be contributing to the different responses between sites.

## 4. Discussion

### 4.1. Endmember generation and spectral unmixing

The unmixing results presented here provided estimates of the fractional cover across Australia with a reasonable accuracy. PV was estimated most accurately, with  $0.131 \leq \text{RMSE} \leq 0.143$  ( $0.651 \leq r^2 \leq 0.696$ ) depending on the sensor used. NPV was estimated less accurately, with  $0.163 \leq \text{RMSE} \leq 0.181$  ( $0.410 \leq r^2 \leq 0.449$ ). BS was estimated with a lower accuracy than PV, but higher than BS: ( $0.130 \leq \text{RMSE} \leq 0.166$  ( $0.542 \leq r^2 \leq 0.724$ )). The most important aspect of this work is the large number of field measurements used, which spans a very large geographic area across 13 years. There are few studies that compare remote sensing estimates from multispectral imagery with field measurements of these three fractions. In most cases the accuracy has been assessed using a small number of sites (i.e., tens or fewer; e.g., Gill & Phinn, 2008; Gill & Phinn, 2009; Guerschman et al., 2009; Okin et al., 2013; corresponding to items #5, 6, 7 and 10 in Table 1, respectively). The only studies which used a large number of sites (i.e., hundreds) were also in Australia and used a subset of the measurements used here. Guerschman et al. (2012) (#9 in Table 1) improved the model of Guerschman et al. (2009) (#7 in Table 1) and achieved RMSE of 0.148, 0.212 and 0.176 for PV, NPV and BS, respectively, using MODIS (MCD43A4) data. Here we followed the approach of Scarth et al. (2010) who reported an overall RMSE of 0.118 (using Landsat data), better than what we obtained here (#8 in Table 1). However, Scarth et al. (2010) performed an additional iterative correction for inaccuracies in the observed PV and NPV fractions, based on the assumption that large, opposing errors in the PV/NPV discrimination are due to errors in the field measurements and not in the unmixing models (Scarth, pers. comm.). The same correction was not performed here. One of our goals was to produce a MODIS fractional cover product which improved the performance of those obtained by Guerschman et al. (2009, 2012); and we have achieved such goal.

Time differences may occur between the field observations and the time when a cloud-free image is available. When a large time difference occurs during dynamic changes in fractional cover, such as greening onset or offset or during disturbances such as fire or grazing, an error in the model estimates can be introduced. This is minimised when using MODIS composite products as used here but not when using

Landsat data. We identified some particular cases of large PV overestimation for cropping sites when the observation occurred after harvest, but the Landsat image was acquired a few days earlier when there was high PV or NPV cover at the site. However, a closer inspection shows that there is no clear relationship between time difference in Landsat and model performance (Figure S6) and therefore a correction (or weighting) based on time difference would not appear to provide additional improvements over what we achieved.

Part of the error in the fractional cover estimates could be related to errors in the field measurements. Previous work on the reliability of the star transect methodology has highlighted that the method produces reliable results, particularly if the field staff are well trained and experienced (Trevithick, Muir, & Denham, 2012). While the majority of sites were collected by staff following the national guidelines (Muir et al., 2011) and specifically trained in the method, some observer bias is evident when classifying the fractions. NPV is the most difficult to obtain consistent field data for and estimates can vary considerably between observers. This can result in outliers in the dataset, particularly for PV and NPV. This has been confirmed by field photography at several of the field sites.

The unmixing models developed here derived the endmembers from the entire field observation dataset. The cross-validation ensures that a sub-space of the bands is used which avoids over-fitting. In the cross-validation we found that for the six Landsat variants there was little difference in the RMSE between  $\sim 10$  and  $\sim 23$  singular values and for the two MODIS products such region was between  $\sim 10$  and  $\sim 34$  singular values (Fig. 6). Similar results were found by Scarth et al. (2010) who argued that this demonstrates the value of adding the band transformations as a way to account for non-linear spectral mixing and band interactions and also demonstrates the effects of over-fitting when the dimensionality increases beyond  $\sim 23$  (in Landsat) or  $\sim 34$  (in MODIS).

In this study only one endmember per fractional cover type is selected. There are alternatives to this method, such as finding the pure pixels (which Fig. 2 suggests they exist in this dataset) (see Plaza, Martinez, Perez, and Plaza (2004) for a comprehensive review). Additionally, each fraction could be represented by more than one endmember and a multiple endmember spectral unmixing approach could be tested (Ballantine, Okin, Prentiss, & Roberts, 2005; Okin et al., 2013; Roberts et al., 1998). These options would require a different mathematical approach and will be tried in future analyses.

### 4.2. Site heterogeneity

Our results support the hypothesis that site heterogeneity is a key factor that influences model performance; to date not assessed by others. The field measurement protocol was designed specifically to be used with Landsat imagery and therefore samples an area of approximately one hectare, equivalent to nine ( $3 \times 3$ ) Landsat pixels. When a sensor with a pixel size  $> 1 \text{ ha}$  is used with these field data a mismatch between the spatial support of the observations and the satellite sampling occurs as the field measurements does not accurately represent the area of the per-pixel satellite measurement. When we degraded Landsat's spatial resolution (by aggregating Landsat surface reflectance to pixels of increasing size) and maintained the same bands, the model goodness of fit decreased (Fig. 8), as expected. The direct correlation between model residuals and a metric of site heterogeneity further supports the site heterogeneity-model performance hypothesis (Table 2 and Figure S2). The more heterogeneous sites had, on average, higher model residuals (in absolute values) particularly in MODIS-derived models for NPV and BS.

The goodness of fit of the two MODIS-based models was lower than the performance of the model with Landsat resampled to a similar resolution as MODIS ( $L_{17} \times 17$ ) particularly for BS (Fig. 8). This suggests that there are factors other than the spatial resolution that causes the MODIS product to perform worse than Landsat, once the change in spatial support is taken into account. Those may be related to the use of off-nadir data (in MOD09A1) or a long (16-day) period of integration of surface

reflectance (in the case of MCD43A4) during times of rapid fractional cover changes. The additional band in MODIS (Band 5, ~1200 nm) did not provide an advantage over Landsat with the unmixing approach taken here.

Amongst the two MODIS products tested, the goodness of fit of MOD09A1 was slightly better than the MCD43A4. This result is surprising as based on previous work we had expected the opposite. To our knowledge, this is the first time that both MODIS products are compared for the estimation of fractional cover, but the two products have been tested for other applications. For example, [Jurdao, Yebra, Chuvieco, and Guerschman \(2013\)](#) found MCD43A4 better suited than MOD09A1 for estimating woodland moisture content using radiative transfer models. The MCD43A4 product was also better than MOD09A1 for fusing MODIS-Landsat imagery ([Bhandari, Phinn, & Gill, 2012](#); [Walker, de Beurs, Wynne, & Gao, 2012](#)). MCD43A4 (MODIS NBAR) estimates a surface reflectance as if it was observed from nadir, therefore minimising viewing angle effects that affect MOD09A1. On the other hand, MCD43A4 integrates observations over a 16-day period, while MOD09A1 picks the best observation within an 8-day period (lowest viewing angle and cloud-free) which may explain the difference. However, the lack of significant correlation between the time difference between the dates of field observation and the Landsat acquisition suggests that the time of MODIS integration may not significantly affect the model performance. Additional research is needed to understand the causes of the differences between the two MODIS products.

#### 4.3. Soil colour and soil moisture

[Guerschman et al. \(2009\)](#) suggested that soil colour and soil moisture changes did not overly affect their algorithm as these two properties affected total albedo but not the shape of the surface reflectance in the bands detected by Landsat or MODIS sensors. Similarly, [Gill and Phinn \(2008\)](#) found no strong influence of soil colour on their method. As the algorithm of [Guerschman et al. \(2009\)](#) was based on two indices (i.e., NDVI and the ratio of MODIS bands 7 and 6) they argued that changing soil properties would not have a significant effect on the model estimates. However, [Guerschman et al. \(2012\)](#) showed that as soils get wet their surface reflectance in 2100 nm decreases more rapidly than the surface reflectance at 1600 nm, therefore affecting their model's ability to accurately distinguish NPV and BS. Results reported here show that neither soil colour nor soil moisture affected the model goodness of fit when the whole dataset is used for the analysis. However, when the analysis is stratified using only those sites with >50% observed BS (assuming that in those sites the effects of soil reflectance on the models will be stronger), a weak yet significant ( $p < 0.05$ ) correlation was found. BS tends to be estimated with less error in brighter and in dryer soils ([Table 2](#) and Figures S2 to S4). To a lesser extent the same occurs with PV and NPV (in sites with BS > 50%) which have (in some cases) a weak trend to display lower error residuals in bright and dry soils (Figures S2 to S4). These results may suggest that dark and/or wet soils tend to produce slightly higher estimation errors in the retrieved fractions, possibly because in such situations the surface reflectance of soils and vegetation (particularly NPV) is more alike. We stress, however, that the correlations are weak and not necessarily show a causal relationship.

There are three possible reasons why we did not find any strong correlation between soil moisture and model performance as expected. Firstly, it is possible that the spatial resolution of the two alternative sources of soil moisture information is not appropriate for this analysis. Both the passive microwave and the AWRA-L model outputs are very coarse (~12.5 km and 5 km pixel size, respectively). The soil moisture in many, or most, of the field sites may be more variable in space and the data used may not be representative of the conditions found in each site. Spectral measurements in [Guerschman et al. \(2012\)](#) suggests that the surface reflectance of very wet soils is highly similar to NPV

(in Landsat or MODIS bands) and therefore estimation errors for NPV and BS may still occur in very particular situations, not detected by the soil moisture measurements used in this study. Secondly, as noted by [Okin et al. \(2013\)](#), even if the soil is wet in the top few centimetres (~0–5 cm) (as detected by passive microwave sensors and simulated by the AWRA-L model), the surface reflectance measured by optical sensors is influenced only by the soil conditions in the top few millimetres. In arid environments the top few millimetres of soil dries quickly after a rainfall event ([Lobell & Asner, 2002](#)) and therefore not affect soil reflectance as measured by an optical sensor. Thirdly and finally, the factor that may add to the lack of a strong influence of soil moisture on model performance is the presence of cryptogam crust. Based on previous studies which showed an important red-near infrared signal due to chlorophyll activity ([Karnieli, 1997](#); [O'Neill, 1994](#)) here we assumed cryptogam to be part of PV. However, cryptogam spectra have also been found to be highly dynamic depending on moisture conditions and shift quickly from a PV-like spectrum to a NPV-like one ([Karnieli, Kidron, Glaesser, & Ben-Dor, 1999](#)). In this study the number of sites with cryptogam presence is not high (from the 1171 observations, only 116 (9%) had more than 10% cryptogam cover and 36 (3%) had more than 20% cryptogam cover) and therefore we do not expect this to cause an important effect on overall model performance (although those specific sites may be poorly estimated). We conclude that the algorithms used here are not overly affected by soil moisture nor soil colour although we cannot discard some negative effects on model performance, particularly on total vegetation cover (PV + NPV) in dark, wet soils.

#### 4.4. Towards an integrated Landsat–MODIS product

The results presented set the basis for a combined Landsat/MODIS fractional cover product which takes advantage of being calibrated and validated using the same set of field observations. The unmixing models developed here allow fractional cover estimates from the Landsat 5/7 and the MODIS sensor to be generated that are broadly consistent ([Fig. 9](#)). The same approach for deriving endmembers, cross calibrating and unmixing, all using the same field observations was applied. We envisage a combined product which gives flexibility to use MODIS-derived estimates when large areas and high temporal repetition is desired, and Landsat-derived estimates when high spatial resolution is essential and/or when data prior to 2000 is needed. Additionally, this study provides the algorithms needed for implementing a fractional cover product based on a blended Landsat–MODIS product as proposed by [Emelyanova, McVicar, Van Niel, Li, and van Dijk \(2013\)](#). Direct application of the unmixing algorithms developed in this paper to the Operational Land Imager (OLI) sensor on board the Landsat 8 satellite poses a challenge, as the spectral response functions of several bands differ from TM/ETM+. A similar situation occurs with the Visible Infrared Imaging Radiometer Suite (VIIRS) sensor on board the Suomi NPP satellite, which differs in its spectral response functions to the MODIS sensor. In both cases, a radiometric intercomparison and intercalibration (e.g. [Upadhyay et al., 2013](#)) and/or further calibration with new field observations should be done before applying the algorithms presented here.

### 5. Conclusion

We investigated the use of a spectral unmixing algorithm for deriving vegetation fractional cover estimates using a large database of field measurements collected across Australia over ~15 years. For each observation we used surface reflectance data from Landsat TM/ETM+ at the site resolution (averaging a  $3 \times 3$  pixels window) and at a coarser resolution (averaging a  $17 \times 17$  pixel window). We also derived the surface reflectance of each observation as derived from two MODIS products. The main findings are:

- As expected, the goodness of fit of the unmixing models was best when using Landsat surface reflectance from an area corresponding to the field measurements (~1 ha). We obtained a RMSE of 0.112, 0.162 and 0.130 for PV, NPV and BS, respectively.
- Using two alternative sources of MODIS surface reflectance data (MCD43A4 and MOD09A1) we obtained results slightly worse than when using the Landsat surface reflectance degraded to a similar 500 m resolution. The unmixing performed with the MOD09A1 product was slightly better than the one performed with the MCD43A4 product.
- No strong evidence that soil colour or soil moisture overly influence model performance was found. We suggest that the unmixing models are likely insensitive to soil colour and/or that the soil moisture in the top few millimetres of soil, which influence surface reflectance in optical sensors, is decoupled from the soil moisture in the top layer (i.e., a few cm) as measured by passive microwave sensors and estimated by models.
- We set the basis for an operational Landsat/MODIS combined product which would benefit users with varying requirements of spatial resolution, temporal frequency and product latency.
- The analyses performed here include sites from the Australian continent where a comprehensive field measurement database has been collected. The spectral properties of the different elements in the landscape are, in principle, similar across many other regions in the world. While a more comprehensive calibration and validation of these algorithms including more sites on other continents is desired, we propose that the models fitted here could be tested in other regions.

## Acknowledgements

The Australian Government Department of Agriculture through the Ground Cover monitoring for Australia project (<http://www.agriculture.gov.au/abares/aclump/land-cover/ground-cover-monitoring-for-australia>) funded this work and the field site data collection undertaken by state agencies during 2010–2013 and collated the national database. The data were collected by the following state agencies: (i) New South Wales Office of Environment and Heritage; (ii) Northern Territory Department of Land Resource Management; (iii) Queensland Department of Science, Information Technology, Innovation and the Arts; (iv) South Australian Department of Environment, Water and Natural Resources; (v) Tasmanian Department of Primary Industries, Parks, Water and Environment; (vi) Victorian Department of Economic Development, Jobs, Transport and Resources; and (vii) Western Australian Department of Agriculture and Food. Other financial assistance was provided by the Terrestrial Ecosystem Research Network (TERN) AusCover facility ([www.auscover.org.au](http://www.auscover.org.au)), the Australian Centre for Ecological Analysis and Synthesis (ACEAS, [www.aceas.org.au](http://www.aceas.org.au)) and the Sustaining Agriculture Soils and Landscapes Program in the CSIRO Agriculture Flagship.

Mark Berman provided useful comments on the spectral unmixing approach on an early stage of manuscript preparation. We thank Michele Cappellari for his IDL implementation of the bound constrained linear least-squares minimization (BVLS) algorithm which we downloaded from <http://www-astro.physics.ox.ac.uk/~mxc/software/bvls.pro>. We are grateful to David Fanning ([idlcoyote.com](http://idlcoyote.com)) for making IDL more accessible, efficient and fun. He indirectly helped to make all figures of this study better. Finally, we thank the Associate Editor and two anonymous reviewers whose comments helped to improve the quality of this paper.

## Appendix A. Supplementary data

Supplementary data associated with this article can be found in the online version, at <http://dx.doi.org/10.1016/j.rse.2015.01.021>.

## References

- ABARES (2013). *Australian ground cover reference sites database*. Australian Bureau of Agricultural and Resource Economics and Sciences, Canberra, Australia (Retrieved August 29, 2013, from <http://rs.nci.org.au/FcSiteData/>).
- Armston, J. D., Denham, R. J., Danaher, T. J., Scarth, P. F., & Moffitt, T. N. (2009). Prediction and validation of foliage projective cover from Landsat-5 TM and Landsat-7 ETM+ imagery. *Journal of Applied Remote Sensing*, 3(1), 33528–33540. <http://dx.doi.org/10.1117/1.3216031>.
- Asner, G. P., Borghetti, C. E., & Ojeda, R. A. (2003). Desertification in central Argentina: Changes in ecosystem carbon and nitrogen from imaging spectroscopy. *Ecological Applications*, 13(3), 629–648. [http://dx.doi.org/10.1890/1051-0761\(2003\)013\[0629:DCACI\]2.0.CO;2](http://dx.doi.org/10.1890/1051-0761(2003)013[0629:DCACI]2.0.CO;2).
- Asner, G. P., Elmore, A. J., Flint Hughes, R., Warner, A. S., & Vitousek, P. M. (2005). Ecosystem structure along bioclimatic gradients in Hawai'i from imaging spectroscopy. *Remote Sensing of Environment*, 96(3–4), 497–508. <http://dx.doi.org/10.1016/j.rse.2005.04.008>.
- Asner, G. P., & Heidebrecht, K. B. (2002). Spectral unmixing of vegetation, soil and dry carbon cover in arid regions: Comparing multispectral and hyperspectral observations. *International Journal of Remote Sensing*, 23(19), 3939–3958. <http://dx.doi.org/10.1080/0143160110115960>.
- Asner, G. P., & Lobell, D. B. (2000). A biogeophysical approach for automated SWIR unmixing of soils and vegetation. *Remote Sensing of Environment*, 74(1), 99–112. [http://dx.doi.org/10.1016/S0034-4257\(00\)00126-7](http://dx.doi.org/10.1016/S0034-4257(00)00126-7).
- Asrar, G., Myneni, R. B., & Choudhury, B. J. (1992). Spatial heterogeneity in vegetation canopies and remote sensing of absorbed photosynthetically active radiation: A modeling study. *Remote Sensing of Environment*, 41(2–3), 85–103. [http://dx.doi.org/10.1016/0034-4257\(92\)90070-Z](http://dx.doi.org/10.1016/0034-4257(92)90070-Z).
- Ballantine, J. -A. C., Okin, G. S., Prentiss, D. E., & Roberts, D. A. (2005). Mapping North African landforms using continental scale unmixing of MODIS imagery. *Remote Sensing of Environment*, 97(4), 470–483. <http://dx.doi.org/10.1016/j.rse.2005.04.023>.
- Bartley, R., Roth, C. H., Ludwig, J., McJannet, D., Liedloff, A., Corfield, J., et al. (2006). Runoff and erosion from Australia's tropical semi-arid rangelands: Influence of ground cover for differing space and time scales. *Hydrological Processes*, 20(15), 3317–3333. <http://dx.doi.org/10.1002/hyp.6334>.
- Bastin, G., Scarth, P., Chewings, V., Sparrow, A., Denham, R., & Schmidt, M. (2012). Separating grazing and rainfall effects at regional scale using remote sensing imagery: A dynamic reference-cover method. *Remote Sensing of Environment*, 121(0), 443–457 (Retrieved from <http://www.sciencedirect.com/science/article/pii/S0034425712001149>).
- Bhandari, S., Phinn, S., & Gill, T. (2012). Preparing Landsat Image Time Series (LITS) for monitoring changes in vegetation phenology in Queensland, Australia. *Remote Sensing*, 4(12), 1856–1886. <http://dx.doi.org/10.3390/rs4061856>.
- Daughtry, C. S. T., Doraiswamy, P. C., Hunt, E. R., Jr., Stern, A. J., McMurtrey, J. E., III, & Prueger, J. H. (2006). Remote sensing of crop residue cover and soil tillage intensity. *Soil and Tillage Research*, 91(1–2), 101–108. <http://dx.doi.org/10.1016/j.still.2005.11.013>.
- Dobigeon, N., Tourneret, J. -Y., Richard, C., Bermudez, J. C. M., McLaughlin, S., & Hero, A. O. (2014). Nonlinear unmixing of hyperspectral images: Models and algorithms. *Signal Processing Magazine, IEEE*, 31(1), 82–94. <http://dx.doi.org/10.1109/MSP.2013.2279274>.
- Doubková, M., van Dijk, A. I. J. M., Sabel, D., Wagner, W., & Blöschl, G. (2012). Evaluation of the predicted error of the soil moisture retrieval from C-band SAR by comparison against modelled soil moisture estimates over Australia. *Remote Sensing of Environment*, 120, 188–196.
- Dungan, J. L., Perry, J. N., Dale, M. R. T., Legendre, P., Citron-Pousty, S., & Fortin, M. -J. (2002). A balanced view of scale in spatial statistical analysis. *Ecography*, 25(5), 626–640. <http://dx.doi.org/10.1043/1600-0587.2002.250510.x>.
- Eldén, L. (2004). Partial least-squares vs. Lanczos bidiagonalization—I: Analysis of a projection method for multiple regression. *Computational Statistics & Data Analysis*, 46(1), 11–31. [http://dx.doi.org/10.1016/S0167-9473\(03\)00138-5](http://dx.doi.org/10.1016/S0167-9473(03)00138-5).
- Elmore, A. J., Asner, G. P., & Hughes, R. F. (2005). Satellite monitoring of vegetation phenology and fire fuel conditions in Hawaiian drylands. *Earth Interactions*, 9(21), 1–21. <http://dx.doi.org/10.1175/EI160.1>.
- Emelyanova, I. V., McVicar, T. R., Van Niel, T. G., Li, L. T., & van Dijk, A. I. J. M. (2013). Assessing the accuracy of blending Landsat–MODIS surface reflectances in two landscapes with contrasting spatial and temporal dynamics: A framework for algorithm selection. *Remote Sensing of Environment*, 133, 193–209. <http://dx.doi.org/10.1016/j.rse.2013.02.007>.
- Escadafal, R., Girard, M. -C., & Courault, D. (1989). Munsell soil color and soil reflectance in the visible spectral bands of landsat MSS and TM data. *Remote Sensing of Environment*, 27(1), 37–46. [http://dx.doi.org/10.1016/0034-4257\(89\)90035-7](http://dx.doi.org/10.1016/0034-4257(89)90035-7).
- Flood, N., Danaher, T., Gill, T., & Gillingham, S. (2013). An Operational scheme for deriving standardised surface reflectance from Landsat TM/ETM + and SPOT HRG imagery for Eastern Australia. *Remote Sensing*, 5(1), 83–109. <http://dx.doi.org/10.3390/rs5010083>.
- Garrigues, S., Allard, D., Baret, F., & Weiss, M. (2006). Influence of landscape spatial heterogeneity on the non-linear estimation of leaf area index from moderate spatial resolution remote sensing data. *Remote Sensing of Environment*, 105(4), 286–298. <http://dx.doi.org/10.1016/j.rse.2006.07.013>.
- Gill, T., & Phinn, S. (2008). Estimates of bare ground and vegetation cover from Advanced Spaceborne Thermal Emission and Reflection Radiometer (ASTER) short-wave-infrared reflectance imagery. *Journal of Applied Remote Sensing*, 2(1), 23511–23519. <http://dx.doi.org/10.1117/1.2907748>.
- Gill, T. K., & Phinn, S. R. (2009). Improvements to ASTER-derived fractional estimates of bare ground in a savanna rangeland. *Geoscience and Remote Sensing, IEEE Transactions on*. <http://dx.doi.org/10.1109/TGRS.2008.2004628>.
- Guerschman, J. P., Hill, M. J., Renzullo, L. J., Barrett, D. J., Marks, A. S., & Botha, E. J. (2009). Estimating fractional cover of photosynthetic vegetation, non-photosynthetic vegetation and bare soil in the Australian tropical savanna region upscaling the EO-1

- Hyperion and MODIS sensors. *Remote Sensing of Environment*, 113(5), 928–945. <http://dx.doi.org/10.1016/j.rse.2009.01.006>.
- Guerschman, J. P., Oyarzábal, M., Malthus, T., McVicar, T. R., Byrne, G., Randall, L., et al. (2012). Evaluation of the MODIS-based vegetation fractional cover product. Canberra: CSIRO Land and Water Science report, Canberra, Australia, 31 (Retrieved from <http://www.clw.csiro.au/publications/science/2012/SAF-MODIS-fractional-cover.pdf>).
- Jurdao, S., Yebra, M., Chuvieco, E., & Guerschman, J. P. (2013). Regional estimation of woodland moisture content by inverting radiative transfer models. *Remote Sensing of Environment*, 132, 59–70. <http://dx.doi.org/10.1016/j.rse.2013.01.004>.
- Karnieli, A. (1997). Development and implementation of spectral crust index over dune sands. *International Journal of Remote Sensing*, 18(6), 1207–1220. <http://dx.doi.org/10.1080/014311697218368>.
- Karnieli, A., Kidron, G. J., Glaeser, C., & Ben-Dor, E. (1999). Spectral characteristics of cyanobacteria soil crust in semiarid environments. *Remote Sensing of Environment*, 69(1), 67–75. [http://dx.doi.org/10.1016/S0034-4257\(98\)00110-2](http://dx.doi.org/10.1016/S0034-4257(98)00110-2).
- Lawson, C. L. (1995). Solving least squares problems. Solving least squares problems. Society for Industrial and Applied Mathematics, i–xiv. <http://dx.doi.org/10.1137/1.9781611971217.fm>.
- Lawson, C. L., & Hanson, R. J. (1974). *Solving least squares problems*. Vol. 161. (pp. 340). Englewood Cliffs: Prentice-Hall, 340.
- Leys, J., Smith, J., MacRae, C., Rickards, J., Yang, X., & Randall, L. (2009). *Improving the capacity to monitor wind and water erosion: A review*. Canberra: Department of Agriculture, Fisheries and Forestry, 146 (Retrieved from <http://nrmonline.nrm.gov.au/catalog/mql/2243>).
- Liang, S., Fang, H., Chen, M., Shuey, C. J., Walthall, C., & Daughtry, C. (2002). Validating MODIS land surface reflectance and albedo products: Methods and preliminary results. *Remote Sensing of Environment*, 83(1–2), 149–162. [http://dx.doi.org/10.1016/S0034-4257\(02\)00092-5](http://dx.doi.org/10.1016/S0034-4257(02)00092-5).
- Lobell, D. B., & Asner, G. P. (2002). Moisture effects on soil reflectance. *Soil Science Society of America Journal*, 66(3), 722–727 (Retrieved from <https://www.soils.org/publications/ssaj/abstracts/66/3/722>).
- Markham, B. L., Storey, J. C., Williams, D. L., & Irons, J. R. (2004). Landsat sensor performance: History and current status. *Geoscience and Remote Sensing, IEEE Transactions on*. <http://dx.doi.org/10.1109/TGRS.2004.840720>.
- McVicar, T. R., & Jupp, D. L. B. (1998). The current and potential operational uses of remote sensing to aid decisions on drought exceptional circumstances in Australia: A review. *Agricultural Systems*, 57(3), 399–468. [http://dx.doi.org/10.1016/S0308-521X\(98\)00026-2](http://dx.doi.org/10.1016/S0308-521X(98)00026-2).
- McVicar, T. R., Jupp, D. L. B., Reece, P. H., & Williams, N. A. (1996). *Relating LANDSAT TM vegetation indices to in situ leaf area index measurements*. Canberra, Australia: CSIRO Division of Water Resources, 80 (Retrieved from [http://www.clw.csiro.au/publications/technical96/DWR\\_TR96-14.pdf](http://www.clw.csiro.au/publications/technical96/DWR_TR96-14.pdf)).
- McVicar, T. R., Jupp, D. L. B., & Williams, N. A. (1996). *Relating AVHRR vegetation indices to LANDSAT TM leaf area index estimates*. Canberra, Australia: CSIRO Division of Water Resources, 29 (Retrieved from [http://www.clw.csiro.au/publications/technical96/DWR\\_TR-96-15.pdf](http://www.clw.csiro.au/publications/technical96/DWR_TR-96-15.pdf)).
- Mouazen, A. M., Karoui, R., de Baerdemaeker, J., & Ramon, H. (2005). Classification of soil texture classes by using soil visual near infrared spectroscopy and factorial discriminant analysis techniques. *Journal of Near Infrared Spectroscopy*, 13(4), 231–240. <http://dx.doi.org/10.1255/jnis.541>.
- Muir, J., Schmidt, M., Tindall, D., Trevithick, R., Scarth, P., & Stewart, J. (2011). *Field measurement of fractional ground cover: A technical handbook supporting ground cover monitoring for Australia*. 48 (Canberra. Retrieved from [http://data.daff.gov.au/brs/data/warehouse/pe\\_hbgcm9abll07701/HndbkGrndCovMontrng2011\\_1.0.0\\_LR.pdf](http://data.daff.gov.au/brs/data/warehouse/pe_hbgcm9abll07701/HndbkGrndCovMontrng2011_1.0.0_LR.pdf)).
- Munsell Soil Color Charts (1994). *Munsell Color*, NY. revised edition New Windsor, New York: Macbeth Division of Kollmorgen Instruments Corporation.
- O'Neill, A. L. (1994). Reflectance spectra of microphytic soil crusts in semi-arid Australia. *International Journal of Remote Sensing*, 15(3), 675–681. <http://dx.doi.org/10.1080/0143116940854106>.
- Okin, G. S. (2007). Relative spectral mixture analysis – A multitemporal index of total vegetation cover. *Remote Sensing of Environment*, 106(4), 467–479. <http://dx.doi.org/10.1016/j.rse.2006.09.018>.
- Okin, G. S., Clarke, K. D., & Lewis, M. M. (2013). Comparison of methods for estimation of absolute vegetation and soil fractional cover using MODIS normalized BRDF-adjusted reflectance data. *Remote Sensing of Environment*, 130, 266–279. <http://dx.doi.org/10.1016/j.rse.2012.11.021>.
- Okin, G. S., Roberts, D. A., Murray, B., & Okin, W. J. (2001). Practical limits on hyperspectral vegetation discrimination in arid and semiarid environments. *Remote Sensing of Environment*, 77(2), 212–225.
- Paget, M., & King, E. (2008). *MODIS land data sets for the Australian region*. 96 (Canberra, Australia. Retrieved from [https://remote-sensing.nci.org.au/u39/public/html/modis/lpdac-mosaics-cmar/doc/ModisLand\\_PagetKing\\_20081203-final.pdf](https://remote-sensing.nci.org.au/u39/public/html/modis/lpdac-mosaics-cmar/doc/ModisLand_PagetKing_20081203-final.pdf)).
- Penrose, R. (1955). A generalized inverse for matrices. *Mathematical Proceedings of the Cambridge Philosophical Society*, 51(03), 406–413. <http://dx.doi.org/10.1017/S0305004100030401>.
- Phinn, S., Stanford, M., Scarth, P., Murray, A. T., & Shyy, P. T. (2002). Monitoring the composition of urban environments based on the vegetation-impermeable surface-soil (VIS) model by subpixel analysis techniques. *International Journal of Remote Sensing*, 23(20), 4131–4153. <http://dx.doi.org/10.1080/01431160110114998>.
- Plaza, J., Hendrix, E. T., García, I., Martín, G., & Plaza, A. (2012). On endmember identification in hyperspectral images without pure pixels: A comparison of algorithms. *Journal of Mathematical Imaging and Vision*, 42(2–3), 163–175. <http://dx.doi.org/10.1007/s10851-011-0276-0>.
- Plaza, A., Martinez, P., Perez, R., & Plaza, J. (2004). A quantitative and comparative analysis of endmember extraction algorithms from hyperspectral data. *IEEE Transactions on Geoscience and Remote Sensing*, 42(3), 650–663. <http://dx.doi.org/10.1109/TGRS.2003.820314>.
- Post, D. F., Fimbres, A., Matthias, A. D., Sano, E. E., Accioly, L., Batchily, A. K., et al. (2000). Predicting soil albedo from soil color and spectral reflectance data. *Soil Science Society of America Journal*, 64(3), 1027–1034. <http://dx.doi.org/10.2136/sssaj2000.6431027x>.
- Puyou-Lascassies, P., Flouzat, G., Gay, M., & Vignolles, C. (1994). Validation of the use of multiple linear regression as a tool for unmixing coarse spatial resolution images. *Remote Sensing of Environment*, 49(2), 155–166.
- Roberts, D. A., Gardner, M., Church, R., Ustin, S., Scheer, G., & Green, R. O. (1998). Mapping Chaparral in the Santa Monica Mountains using multiple endmember spectral mixture models. *Remote Sensing of Environment*, 65(3), 267–279. [http://dx.doi.org/10.1016/S0034-4257\(98\)00037-6](http://dx.doi.org/10.1016/S0034-4257(98)00037-6).
- Salvador, R., & Pons, X. (1998). On the reliability of Landsat TM for estimating forest variables by regression techniques: A methodological analysis. *IEEE Transactions on Geoscience and Remote Sensing*, 36(6), 1888–1897. <http://dx.doi.org/10.1109/36.729360>.
- Scarth, P., & Phinn, S. (2000). Determining forest structural attributes using an inverted geometric-optical model in mixed eucalypt forests, Southeast Queensland, Australia. *Remote Sensing of Environment*, 71(2), 141–157.
- Scarth, P., Roder, A., & Schmidt, M. (2010). Tracking grazing pressure and climate interaction—The role of Landsat fractional cover in time series analysis. *Proceedings of the 15th Australasian Remote Sensing and Photogrammetry Conference* Australia: Alice Springs. <http://dx.doi.org/10.6084/m9.figshare.94250>.
- Schaaf, C. B., Gao, F., Strahler, A. H., Lucht, W., Li, X., Tsang, T., et al. (2002). First operational BRDF, albedo nadir reflectance products from MODIS. *Remote Sensing of Environment*, 83(1–2), 135–148. [http://dx.doi.org/10.1016/S0034-4257\(02\)00091-3](http://dx.doi.org/10.1016/S0034-4257(02)00091-3).
- Schmidt, M., & Scarth, P. (2009). Spectral mixture analysis for ground-cover mapping. *Innovations in Remote Sensing and Photogrammetry*, 349–359.
- Stewart, J. B., Rickards, J. E., Bordas, V. M., Randall, L. A., & Thackway, R. M. (2009). Ground cover monitoring for Australia—Establishing a coordinated approach to ground cover mapping. *Workshop proceedings* (pp. 44). Canberra: Workshop proceedings, ABARES, Canberra, Australia (Retrieved from [http://adl.brs.gov.au/data/warehouse/pe\\_abares9900179/Groundcover\\_mapping-workshop\\_proc\\_11.pdf](http://adl.brs.gov.au/data/warehouse/pe_abares9900179/Groundcover_mapping-workshop_proc_11.pdf)).
- Trevithick, R., Muir, J., & Denham, R. (2012). The effect of observer experience levels on the variability of fractional ground cover reference data. *16th Australian Remote Sensing and Photogrammetry Conference* (Melbourne, Australia. Retrieved from <http://www.isprs2012.org/abstract/921.asp>).
- Tucker, C. J. (1979). Red and photographic infrared linear combinations for monitoring vegetation. *Remote Sensing of Environment*, 8(2), 127–150. [http://dx.doi.org/10.1016/0034-4257\(79\)90013-0](http://dx.doi.org/10.1016/0034-4257(79)90013-0).
- Upadhye, S., Cao, C., Xiong, X., Blonski, S., Wu, A., & Shao, X. (2013). Radiometric intercomparison between Suomi-NPP VIIRS and Aqua MODIS reflective solar bands using simultaneous nadir overpass in the low latitudes. *Journal of Atmospheric and Oceanic Technology*, 30(12), 2720–2736. <http://dx.doi.org/10.1175/JTECH-D-13-00071.1>.
- Van der Meer, F. (2006). The effectiveness of spectral similarity measures for the analysis of hyperspectral imagery. *International Journal of Applied Earth Observation and Geoinformation*, 8(1), 3–17. <http://dx.doi.org/10.1016/j.jag.2005.06.001>.
- Van Dijk, A. I. J. M., & Renzullo, L. J. (2011). Water resource monitoring systems and the role of satellite observations. *Hydrology and Earth System Sciences*, 15(1), 39–55. <http://dx.doi.org/10.5194/hess-15-39-2011>.
- Vermote, E. F., & Kotchenova, S. (2008). Atmospheric correction for the monitoring of land surfaces. *Journal of Geophysical Research, [Atmospheres]*, 113(D23), D23S90. <http://dx.doi.org/10.1029/2007JD009662>.
- Vermote, E. F., Kotchenova, S. Y., & Ray, J. P. (2011). MODIS surface reflectance user's guide. 1–40 (Retrieved from [http://modis.srltdri.org/products/MOD09\\_UserGuide\\_v1\\_3.pdf](http://modis.srltdri.org/products/MOD09_UserGuide_v1_3.pdf)).
- Viscarra Rossel, R. A., Bui, E. N., de Caritat, P., & McKenzie, N. J. (2010). Mapping iron oxides and the color of Australian soil using visible–near-infrared reflectance spectra. *Journal of Geophysical Research, Earth Surface*, 115(F4), F04031. <http://dx.doi.org/10.1029/2009JF001645>.
- Wagner, W., Lemoine, G., & Rott, H. (1999). A method for estimating soil moisture from ERS scatterometer and soil data. *Remote Sensing of Environment*, 70(2), 191–207. [http://dx.doi.org/10.1016/S0034-4257\(99\)00036-X](http://dx.doi.org/10.1016/S0034-4257(99)00036-X).
- Walker, J. J., de Beurs, K. M., Wynne, R. H., & Gao, F. (2012). Evaluation of Landsat and MODIS data fusion products for analysis of dryland forest phenology. *Remote Sensing of Environment*, 117(0), 381–393. <http://dx.doi.org/10.1016/j.rse.2011.10.014>.
- Whiting, M. L., Li, L., & Ustin, S. L. (2004). Predicting water content using Gaussian model on soil spectra. *Remote Sensing of Environment*, 89(4), 535–552. <http://dx.doi.org/10.1016/j.rse.2003.11.009>.
- Woodcock, C. E., & Strahler, A. H. (1987). The factor of scale in remote sensing. *Remote Sensing of Environment*, 21(3), 311–332.
- Xu, P. (1998). Truncated SVD methods for discrete linear ill-posed problems. *Geophysical Journal International*, 135(2), 505–514. <http://dx.doi.org/10.1046/j.1365-246X.1998.00652.x>.
- Yebra, M., Chuvieco, E., & Riaño, D. (2008). Estimation of live fuel moisture content from MODIS images for fire risk assessment. *Agricultural and Forest Meteorology*, 148(4), 523–536. <http://dx.doi.org/10.1016/j.agrformet.2007.12.005>.

## **Supplementary material**

Title: Assessing the Effects of Site Heterogeneity and Soil Properties when Unmixing Photosynthetic Vegetation, Non-Photosynthetic Vegetation and Bare Soil Fractions from Landsat and MODIS Data

Authors: Juan P. Guerschman, Peter Scarth, Tim R. McVicar, Luigi J. Renzullo, Tim J. Malthus, Jane B. Stewart, Jasmine E. Rickards, and Rebecca Trevithick

# 1 Endmember derivation and unmixing approach

## 1.1 Linear Spectral Unmixing

Linear mixing models represent an observed spectral response as a linear combination of 'pure spectra', the endmembers, for each land cover type (class) of interest within the instantaneous view of the sensor. Mathematically we write:

$$x_k = M^T f_k + \epsilon \quad (\text{S1})$$

where  $x_k$  is a  $b \times 1$  vector representing the observed signal over  $b$  band for the  $k$ th sample or site;  $f_k$  is a  $c \times 1$  vector containing the fractions (0 – 1) of the land cover types for the  $k$ th sample or site; and  $M$  is the  $c \times b$  matrix with the rows representing the endmember spectra for each cover class. The random error term,  $\epsilon$ , is often assumed to be normally distributed with zero mean and homoscedastic with variance  $\sigma^2$ .

For convenience we can denote the collection spectra and field measured fractions of cover, for  $n$  sites, in their respective matrix form. We define,

$$X = [x_1, x_2, \dots, x_k, \dots, x_n]^T,$$

and

$$F = [f_1, f_2, \dots, f_k, \dots, f_n]^T,$$

which allows us to express Eq. (S1) as

$$X = FM. \quad (\text{S2})$$

The fractions of cover,  $f_k$ , determine the magnitude of the contribution that a given endmember has on the overall measured signal at a given location. The ultimate application of linear unmixing algorithms is to estimate fractions of cover given satellite-measured signal and a set of endmember spectra for an arbitrary location in the landscape. The challenge, however, is that endmember spectra are seldom known *a priori*. In this paper we used ground measured fractions of cover with coincident satellite-derived reflectance spectra to infer the endmember spectra for PV, NPV and BS cover types across the Australian landscape. We then apply the derived endmember spectra in linear mixing model with observed reflectance spectra (including band transformations) to obtain estimates of fractions of cover in the landscape. In the following we describe two approaches to

infer the spectral endmembers, and highlight the differences between the methods employed in this paper (Section 1.3) and the more traditional approach (Section 1.2).

## 1.2 Direct inversion

An approach to infer endmember spectra is via the direct inversion of Eq. (S2). By treating the matrix of fractional cover from field observations as the independent (explanatory or predictor) variable and matrix of satellite spectral data as dependent (response) variable, the least squares solution for the endmembers is given as:

$$M = (F^T F)^{-1} F^T X. \quad (\text{S3})$$

The first term on the left-hand side of Eq. (S3) is the Moore-Penrose pseudo-inverse of  $F$  which we denote as  $F^+$ .

## 1.3 Inverse operator

We could consider an *inverse operator* approach to inferring  $M$  in Eq. (S2) and ask: what is the form of a matrix  $A$  such that  $A M = I$ , where  $I$  is a  $b \times b$  identity matrix. The matrix  $A$  is the inverse operator which, after some simple matrix algebra, we can obtain as:

$$A = (X^T X)^{-1} X^T F. \quad (\text{S4})$$

where the  $X$  terms of Eq. (S4) represent the Moore-Penrose pseudoinverse of the spectra data, which we denote as  $X^+$ . An important feature of the inverse operator method is that it can accommodate an increase in dimensionality of the spectral data, either through the addition of spectral bands or inclusion of band transformations and interaction terms in the construction of the design matrix (i.e.,  $X$ ). With increased dimensionality, however, there is a need to deal with collinearity in the spectral data and dimensional reduction methods are required. In this work we have used truncated singular value decomposition (SVD) in the calculation of  $X^+$  and derived the optimum truncation value using a cross-validation procedure (Figure 4 and 5 in the paper). Having calculated the inverse operator,  $A = X^+ F$ , we can estimate  $M$  as,

$$A^+ A M = A^+ \Rightarrow M = A^+,$$

which gives

$$M = (X^+ F)^+. \quad (\text{S5})$$

We can show how Eq. (S5) differs from Eq. (S3) by expressing  $X$  in its SVD form, that is

$$X = UDV^T \quad (\text{S6})$$

where  $U$  is an  $n \times b$  matrix whose columns are the left singular vectors of  $X$ ,  $D$  is a  $b \times b$  diagonal matrix of singular values, and  $V$  is a  $b \times b$  matrix whose columns are the right singular vectors. Note that  $V^T V = VV^T = I_{(b \times b)}$  and  $U^T U = I_{(b \times b)}$  (where  $I_{(b \times b)}$  is  $(b \times b)$  identity matrix), however,  $UU^T$  does not result in an identity matrix. Using Eq. (S6) we obtain the pseudoinverse of  $X$  as,

$$X^+ = (X^T X)^{-1} X^T = VD^{-1}U^T. \quad (\text{S7})$$

Substituting Eq. (S7) into Eq. (S5) gives

$$\begin{aligned} M &= (VD^{-1}U^T F)^+ \\ &= (F^T U D^{-1} V^T V D^{-1} U^T F)^{-1} F^T U D^{-1} V^T \\ &= (F^T U U^T F)^{-1} F^T U D V^T \\ &\Rightarrow M = (F^T U U^T F)^{-1} F^T X. \end{aligned} \quad (\text{S8})$$

We can see that Eq. (S8) differs from Eq. (S3) by the term  $U^T F$ . Note that the columns of  $U$  represent the orthonormal basis vectors spanning the so-called *range* of  $X$ , that is a lower dimensional subspace of  $n$ -dimensional space. The interpretation of  $U^T F$ , therefore, is that it represents a mapping of the  $n \times c$  matrix of fractional cover,  $F$ , onto a lower dimensional space of spectral data matrix,  $X$ .

## 1.4 Estimation of cover fractions

Having calculated the endmember matrix,  $M$ , the next step is to compute the fractions of cover, under the constraints that  $f_i > 0$  for  $i = 1, \dots, c$  and that  $\sum_{i=1}^c f_i = 1$ . To impose the sum-to-one constraint, the linear mixing model is written as,

$$[X, \delta 1^n] = F[M, \delta 1^c], \quad (\text{S9})$$

where  $1^n$  and  $1^c$  vectors of 1's with dimensions of  $n$  and  $c$ , respectively, and  $\delta$  is a parameter that weights the strength of the sum-to-one constraint. To find  $F$ , we have chosen to employ a non-negative least squares (NNLS) solution to Eq. (S9).

## 1.5 Comparison of alternative inversions on the spectral unmixing results

In this paper we derive the endmembers array  $M$  as per Eq (S5) and not with the more widely used direct inversion (Eq S3). We have demonstrated in the previous sections why the  $M$  array obtained in each case differ. Another innovation we introduced in this paper is the use of a number of band transforms and two-band ratios, so the  $b$  dimension of the  $X$  (and  $M$ ) arrays goes from 6 to 63 in the case of the Landsat TM and ETM<sup>+</sup> sensor (7 to 84 in the case of MODIS). The cross-validation step

provides an optimum truncation point when computing  $X^+$  and then ensures that the addition of extra bands does lead to an improvement due to the addition of real information (non-linearities in the spectral mixing) and not due to overfitting (Figures 4 and 5 in the paper).

In order to illustrate the individual effects of the two alternative ways of obtaining the *Marray* and the introduction of the band ratios and transforms, we repeated the process of deriving the endmembers and producing the unmixing to obtain the fractional cover estimates in four alternative ways (Table S1). In each case we calculated the RMSE for each fraction. We show the resulting *M* array in each one of the four cases. The upper left case of Table S1 corresponds to the approach taken in the paper.

The results of this refined spectral unmixing are better when the *Marray* is obtained as per equation S5 (Table S1, top line) compared to results when applying the more traditional approach (Table S1, bottom line). The main reason is that the noise contained in the Landsat data is reduced when the pseudo-inverse of  $X$  is calculated which does not occur in the direct inversion (Eq S3). When additional band transforms are included the unmixing results in better agreement with the observed fractions, particularly for the PV and BS fractions. When the *Marray* is obtained using equation S3 there is lower agreement (higher RMSE) between the estimated and observed cover fractions. Unlike the previous case, the addition of band transforms results in additional degradation of the agreement between observed and estimated cover fractions, likely due to the enhancement in the satellite data noise.

The calculation of the *M* array using eq S3, and without including the band transforms yields endmembers in reflectance units, which are easy to interpret in physical terms (lower right case in table S1). We stress that using such endmembers does not produce the best unmixing results, as can be observed by comparing with the results from the *M* array obtained with Eq S4 (top right case in table S1).

We provide the full contents of the *M* array actually used in this paper using the four surface reflectance data sources in table S2. Finally, Figure S1 repeats the calculation of the *M* array with the direct inversion and no additional band transforms (as in the lower right case of Table S1) for the four surface reflectance data sources.

**Table S1: Plots showing the endmembers array M and root mean square error (RMSE) for the unmixed fractions of cover using four alternative ways of deriving the endmembers array M. Green, red and blue dots and lines correspond to the PV, NPV and BS fractions respectively.**

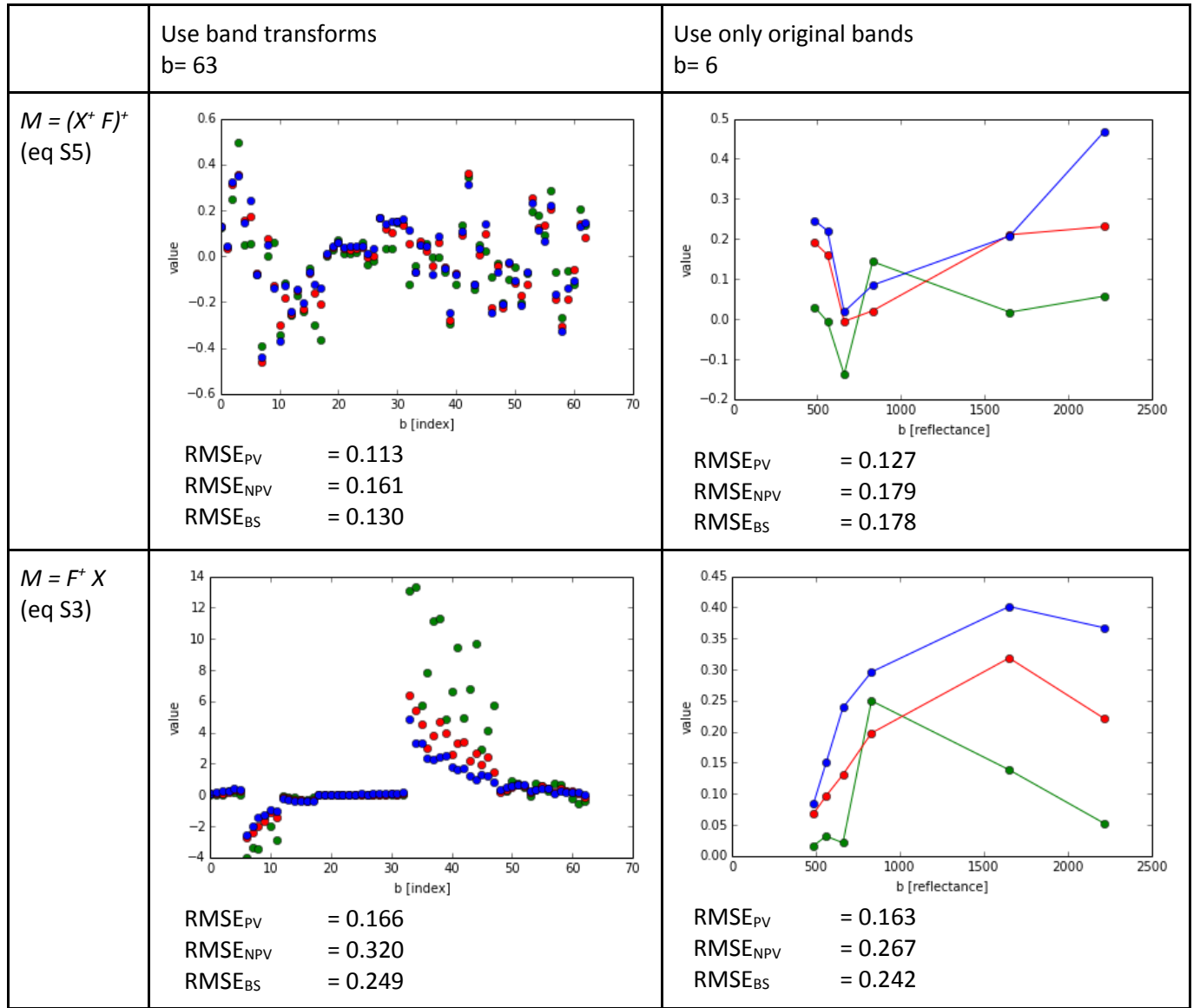


**Table S2: Endmembers (M array) obtained by applying the Moore-Penrose pseudoinverse of the A array, as per equation 16 (S5). B1 to B7 correspond to the surface reflectance bands (only B1 to B6 for Landsat) and ln(Bx) is the natural logarithm of band x.**

Band/ band transform/ band index	Landsat 3x3			Landsat 17x17			MCD43A4			MOD09A1		
	PV	NPV	BS	PV	NPV	BS	PV	NPV	BS	PV	NPV	BS
B1	0.221	0.195	0.185	0.227	0.202	0.178	0.368	0.429	0.434	0.166	0.196	0.198
B2	0.159	0.124	0.133	0.270	0.224	0.206	0.475	0.443	0.433	0.247	0.197	0.237
B3	0.319	0.353	0.352	0.434	0.435	0.400	0.223	0.219	0.207	0.100	0.074	0.078
B4	0.278	0.205	0.219	0.278	0.270	0.297	0.309	0.328	0.328	0.105	0.078	0.068
B5	0.110	0.208	0.196	0.065	0.155	0.140	0.502	0.480	0.441	0.292	0.346	0.357
B6	0.240	0.313	0.373	0.311	0.303	0.347	0.313	0.391	0.324	0.189	0.262	0.217
B7							0.221	0.232	0.331	0.052	0.037	0.069
ln(B1)	-0.004	-0.014	-0.025	-0.346	-0.303	-0.271	-0.127	-0.062	-0.078	0.018	0.095	0.083
ln(B2)	-0.458	-0.489	-0.451	-0.510	-0.504	-0.431	-0.166	-0.302	-0.293	-0.028	-0.161	-0.130
ln(B3)	0.003	0.057	0.027	-0.208	-0.045	-0.023	-0.198	-0.283	-0.354	-0.130	-0.178	-0.194
ln(B4)	-0.102	-0.214	-0.191	-0.284	-0.360	-0.278	-0.343	-0.327	-0.300	-0.196	-0.236	-0.266
ln(B5)	-0.432	-0.344	-0.399	-0.750	-0.607	-0.580	-0.208	-0.272	-0.308	-0.181	-0.135	-0.150
ln(B6)	-0.120	-0.187	-0.130	-0.415	-0.388	-0.270	-0.324	-0.302	-0.398	-0.091	-0.035	-0.103
ln(B7)							-0.247	-0.333	-0.256	-0.132	-0.206	-0.157
ln(B1)*B1	-0.357	-0.349	-0.349	-0.327	-0.334	-0.328	-0.437	-0.434	-0.398	-0.327	-0.348	-0.329
ln(B2)*B2	-0.274	-0.258	-0.265	-0.288	-0.291	-0.289	-0.289	-0.280	-0.266	-0.204	-0.208	-0.178
ln(B3)*B3	-0.370	-0.353	-0.333	-0.306	-0.336	-0.318	-0.380	-0.376	-0.351	-0.263	-0.265	-0.257
ln(B4)*B4	-0.309	-0.295	-0.285	-0.302	-0.278	-0.255	-0.368	-0.379	-0.367	-0.251	-0.254	-0.237
ln(B5)*B5	-0.411	-0.277	-0.244	-0.376	-0.307	-0.275	-0.259	-0.258	-0.254	-0.162	-0.131	-0.111
ln(B6)*B6	-0.478	-0.319	-0.259	-0.302	-0.271	-0.235	-0.422	-0.355	-0.340	-0.311	-0.261	-0.264
ln(B7)*B7							-0.576	-0.500	-0.423	-0.414	-0.391	-0.360
B1*B2	0.047	0.005	-0.014	0.076	0.042	0.011	0.157	0.179	0.185	0.062	0.060	0.072
B1*B3	0.067	0.033	0.013	0.099	0.069	0.038	0.063	0.070	0.073	-0.002	-0.012	-0.008
B1*B4	0.096	0.046	0.025	0.105	0.071	0.043	0.091	0.111	0.119	-0.004	-0.011	-0.008
B1*B5	0.055	0.035	0.015	0.078	0.053	0.022	0.133	0.176	0.180	0.041	0.072	0.073
B1*B6	0.054	0.027	0.018	0.094	0.061	0.038	0.058	0.130	0.138	-0.017	0.018	0.018
B1*B7							0.014	0.065	0.116	-0.048	-0.043	-0.018
B2*B3	0.051	0.022	0.010	0.131	0.093	0.064	0.103	0.097	0.094	0.031	0.012	0.018
B2*B4	0.073	0.019	0.007	0.131	0.088	0.065	0.141	0.145	0.148	0.034	0.008	0.014
B2*B5	0.002	-0.006	-0.014	0.071	0.053	0.030	0.236	0.221	0.212	0.161	0.154	0.177
B2*B6	0.012	-0.005	0.003	0.111	0.074	0.061	0.166	0.188	0.176	0.093	0.104	0.108
B2*B7							0.106	0.114	0.153	0.041	0.021	0.049
B3*B4	0.140	0.107	0.091	0.205	0.176	0.147	0.052	0.054	0.054	-0.002	-0.018	-0.015
B3*B5	0.030	0.076	0.073	0.108	0.130	0.107	0.107	0.104	0.097	0.017	0.011	0.011
B3*B6	0.037	0.065	0.085	0.168	0.150	0.142	0.078	0.087	0.081	0.002	-0.003	-0.006
B3*B7							0.054	0.060	0.072	-0.026	-0.039	-0.031
B4*B5	0.080	0.070	0.059	0.043	0.058	0.058	0.141	0.152	0.151	0.025	0.021	0.015
B4*B6	0.098	0.071	0.085	0.160	0.127	0.130	0.097	0.128	0.128	-0.001	0.001	-0.008
B4*B7							0.065	0.086	0.114	-0.033	-0.046	-0.034
B5*B6	-0.092	0.039	0.080	0.019	0.063	0.081	0.138	0.193	0.164	0.104	0.178	0.159
B5*B7							0.052	0.087	0.134	0.007	0.034	0.053
B6*B7							-0.085	0.001	0.056	-0.108	-0.069	-0.053
ln(B1)*ln(B2)	-0.003	-0.031	-0.031	-0.093	-0.143	-0.149	-0.043	-0.057	-0.095	0.192	0.265	0.247
ln(B1)*ln(B3)	0.003	0.018	0.005	-0.146	-0.007	0.047	0.023	0.069	0.104	0.163	0.169	0.197
ln(B1)*ln(B4)	-0.018	-0.042	-0.020	-0.407	-0.400	-0.318	0.466	0.486	0.439	-0.106	-0.057	-0.094
ln(B1)*ln(B5)	-0.083	-0.060	-0.082	0.236	-0.002	-0.081	-0.315	-0.260	-0.298	-0.056	0.008	-0.009
ln(B1)*ln(B6)	0.091	0.114	0.124	0.100	0.193	0.168	-0.305	-0.214	-0.332	-0.242	-0.227	-0.222
ln(B1)*ln(B7)							0.007	-0.133	-0.025	0.124	-0.006	0.000
ln(B2)*ln(B3)	-0.041	-0.009	-0.011	0.319	0.153	0.072	0.066	0.031	0.043	0.197	0.165	0.202
ln(B2)*ln(B4)	-0.266	-0.244	-0.208	0.046	0.090	0.093	0.065	0.150	0.169	-0.221	-0.279	-0.255
ln(B2)*ln(B5)	-0.111	-0.080	-0.089	-0.292	-0.131	-0.077	0.084	0.046	0.004	0.208	0.223	0.217
ln(B2)*ln(B6)	0.025	-0.010	0.004	-0.142	-0.027	0.046	0.004	-0.033	0.092	-0.386	-0.340	-0.320
ln(B2)*ln(B7)							-0.119	-0.186	-0.237	-0.011	-0.148	-0.186
ln(B3)*ln(B4)	0.413	0.418	0.362	0.625	0.570	0.457	-0.363	-0.413	-0.425	-0.129	-0.179	-0.205
ln(B3)*ln(B5)	-0.207	-0.194	-0.196	-0.480	-0.199	-0.207	0.098	-0.003	-0.016	-0.236	-0.205	-0.177
ln(B3)*ln(B6)	0.125	0.073	0.096	0.041	-0.122	-0.066	0.059	0.012	-0.041	0.192	0.158	0.112

Band/ band transform/ band index	Landsat 3x3			Landsat 17x17			MCD43A4			MOD09A1		
	PV	NPV	BS	PV	NPV	BS	PV	NPV	BS	PV	NPV	BS
ln(B3)*ln(B7)							0.087	0.135	0.096	-0.208	-0.144	-0.150
ln(B4)*ln(B5)	0.154	0.154	0.175	-0.550	-0.402	-0.191	-0.111	-0.101	-0.072	-0.012	-0.078	-0.131
ln(B4)*ln(B6)	-0.214	-0.272	-0.269	0.042	-0.092	-0.164	-0.108	-0.092	-0.052	0.105	0.112	0.113
ln(B4)*ln(B7)							-0.071	-0.020	0.034	0.190	0.274	0.339
ln(B5)*ln(B6)	-0.045	-0.039	-0.057	0.042	-0.015	-0.043	0.168	0.232	0.282	0.271	0.334	0.346
ln(B5)*ln(B7)							0.127	0.141	0.137	0.014	-0.006	0.020
ln(B6)*ln(B7)							0.016	0.002	-0.030	-0.093	-0.084	-0.102
[(B2-B1)/(B2+B1)]	-0.205	-0.218	-0.196	-0.086	-0.102	-0.080	-0.108	-0.230	-0.203	0.051	-0.076	-0.059
[(B3-B1)/(B3+B1)]	0.029	0.045	0.038	0.035	0.151	0.169	-0.096	-0.179	-0.209	-0.010	-0.056	-0.054
[(B4-B1)/(B4+B1)]	0.100	0.017	0.026	0.115	0.000	0.015	-0.131	-0.158	-0.138	-0.114	-0.175	-0.186
[(B5-B1)/(B5+B1)]	-0.182	-0.133	-0.170	-0.133	-0.126	-0.149	-0.204	-0.256	-0.263	-0.177	-0.196	-0.212
[(B6-B1)/(B6+B1)]	-0.100	-0.152	-0.098	-0.021	0.009	0.040	-0.242	-0.256	-0.305	-0.118	-0.143	-0.166
[(B7-B1)/(B7+B1)]							-0.131	-0.202	-0.153	-0.085	-0.178	-0.137
[(B3-B2)/(B3+B2)]	0.218	0.251	0.218	0.138	0.223	0.201	-0.183	-0.121	-0.151	-0.140	-0.075	-0.082
[(B4-B2)/(B4+B2)]	0.263	0.206	0.192	0.203	0.124	0.113	-0.077	0.008	0.003	-0.178	-0.106	-0.139
[(B5-B2)/(B5+B2)]	0.014	0.077	0.009	-0.218	-0.100	-0.110	-0.025	0.007	-0.015	-0.028	0.053	0.014
[(B6-B2)/(B6+B2)]	0.122	0.063	0.083	-0.024	0.029	0.061	-0.035	0.031	-0.033	-0.009	0.087	0.030
[(B7-B2)/(B7+B2)]							0.115	0.103	0.129	0.018	0.074	0.073
[(B4-B3)/(B4+B3)]	0.086	-0.031	-0.008	0.102	-0.062	-0.050	-0.050	-0.007	0.037	-0.097	-0.113	-0.139
[(B5-B3)/(B5+B3)]	-0.280	-0.291	-0.305	-0.426	-0.369	-0.351	0.122	0.114	0.114	-0.105	-0.055	-0.082
[(B6-B3)/(B6+B3)]	-0.119	-0.218	-0.160	-0.169	-0.225	-0.163	0.063	0.096	0.062	-0.004	0.029	-0.023
[(B7-B3)/(B7+B3)]							0.074	0.105	0.138	-0.102	-0.117	-0.092
[(B5-B4)/(B5+B4)]	-0.133	-0.082	-0.133	-0.261	-0.147	-0.174	-0.012	-0.045	-0.066	0.016	0.057	0.047
[(B6-B4)/(B6+B4)]	0.112	0.035	0.018	-0.088	-0.022	0.010	-0.044	-0.044	-0.092	0.143	0.200	0.185
[(B7-B4)/(B7+B4)]							0.021	-0.006	0.015	0.115	0.121	0.190
[(B6-B5)/(B6+B5)]	0.217	0.132	0.182	0.179	0.113	0.170	-0.039	-0.002	-0.041	0.036	0.044	0.022
[(B7-B5)/(B7+B5)]							0.067	0.006	0.075	0.131	0.074	0.101
[(B7-B6)/(B7+B6)]							0.069	-0.005	0.103	-0.004	-0.069	-0.013

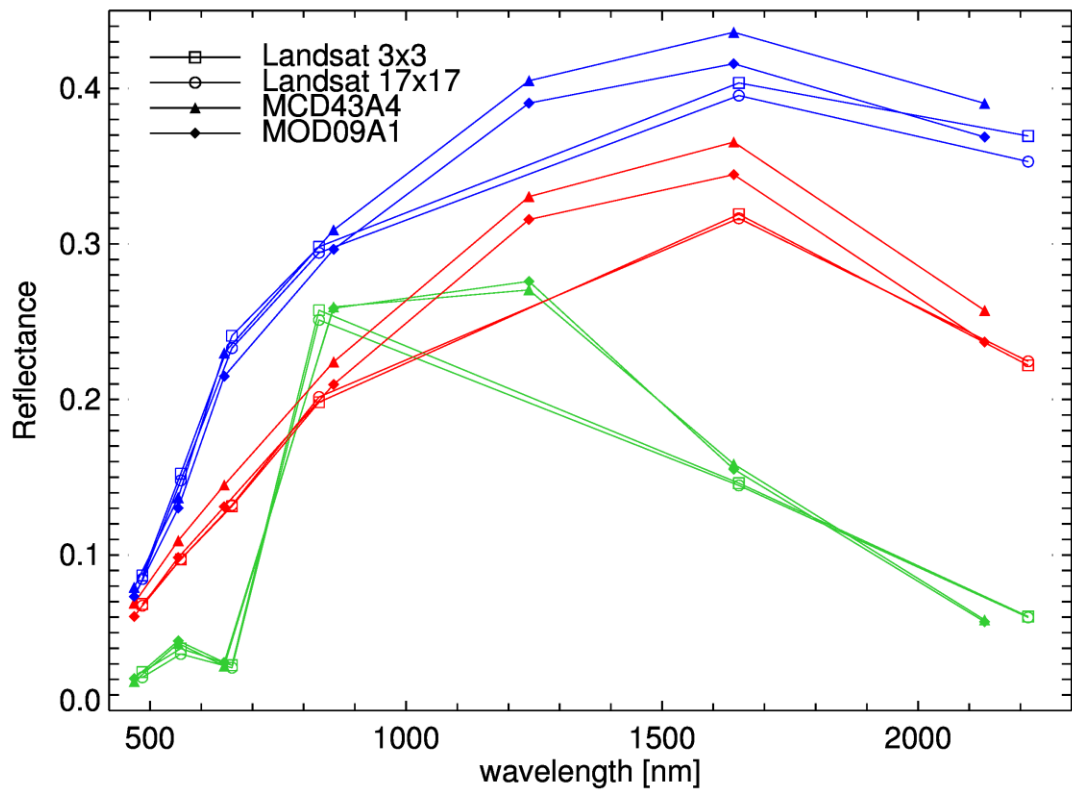


**Figure S1:** Endmembers for the photosynthetic vegetation (green), non-photosynthetic vegetation (red) and bare soil (blue) for the Landsat 3x3, Landsat 17x17, MCD43A4 and MOD09A1 surface reflectance generated by analogy to the classic unmixing approach (equation 17 and S3):  $M = F^+ X$  without including the band transforms. Note that the actual endmembers we used in this paper were obtained with a different approach and are shown in Table S1.

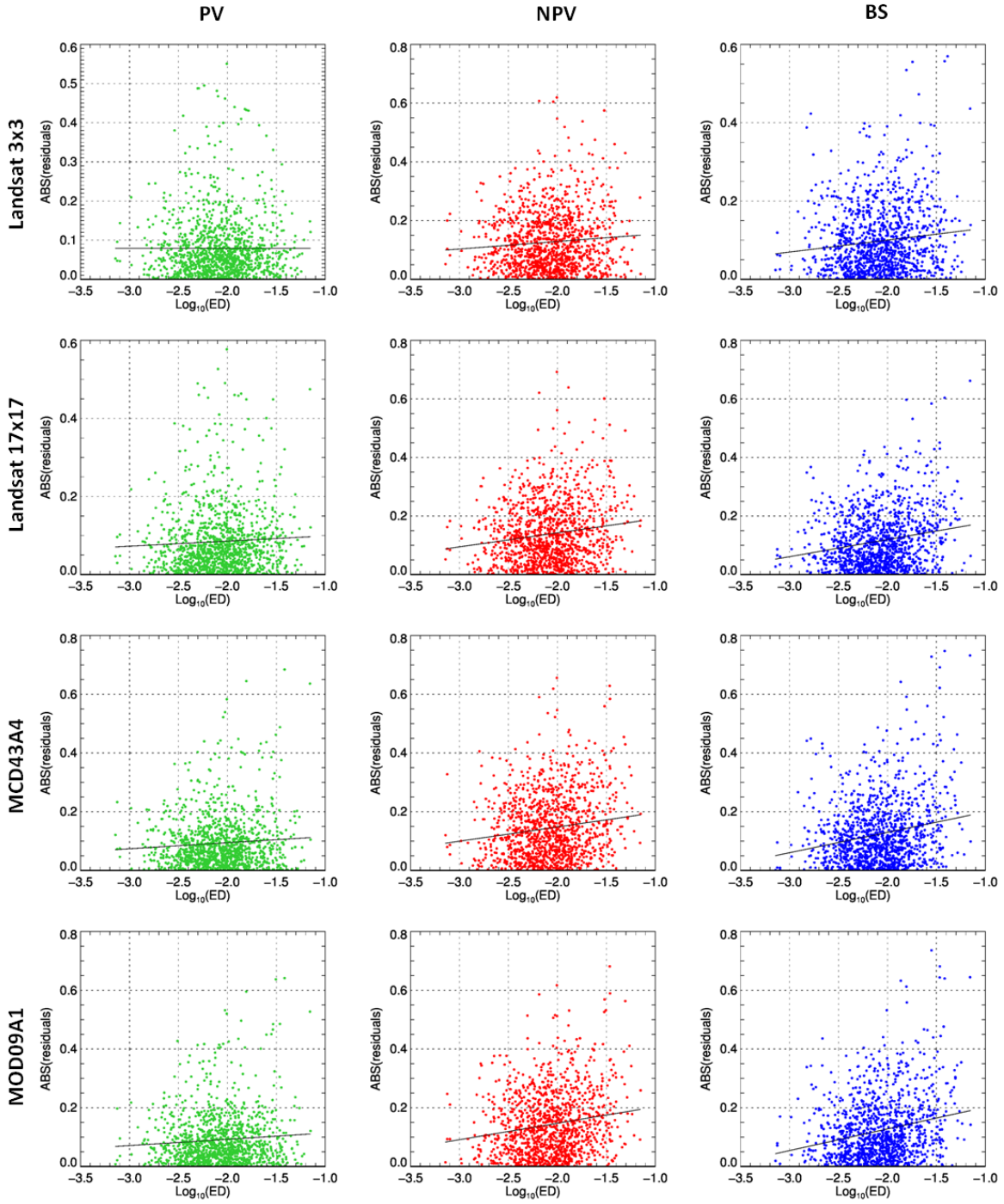


**Figure S2: Scatterplots of the absolute value of model residuals ( $|\text{estimated}-\text{observed}|$ ) and the logarithm of the Euclidean distance between the reflectance in a  $3 \times 3$  pixel window and a  $17 \times 17$  pixel window used as a quantification of site heterogeneity. Landsat 3x3 (top row), Landsat 17x17 (second row), MCD43A4 (third row) and MOD09A1 (bottom row). The red line shows the linear fit. Full statistics for these regressions are provided in Table 2.**

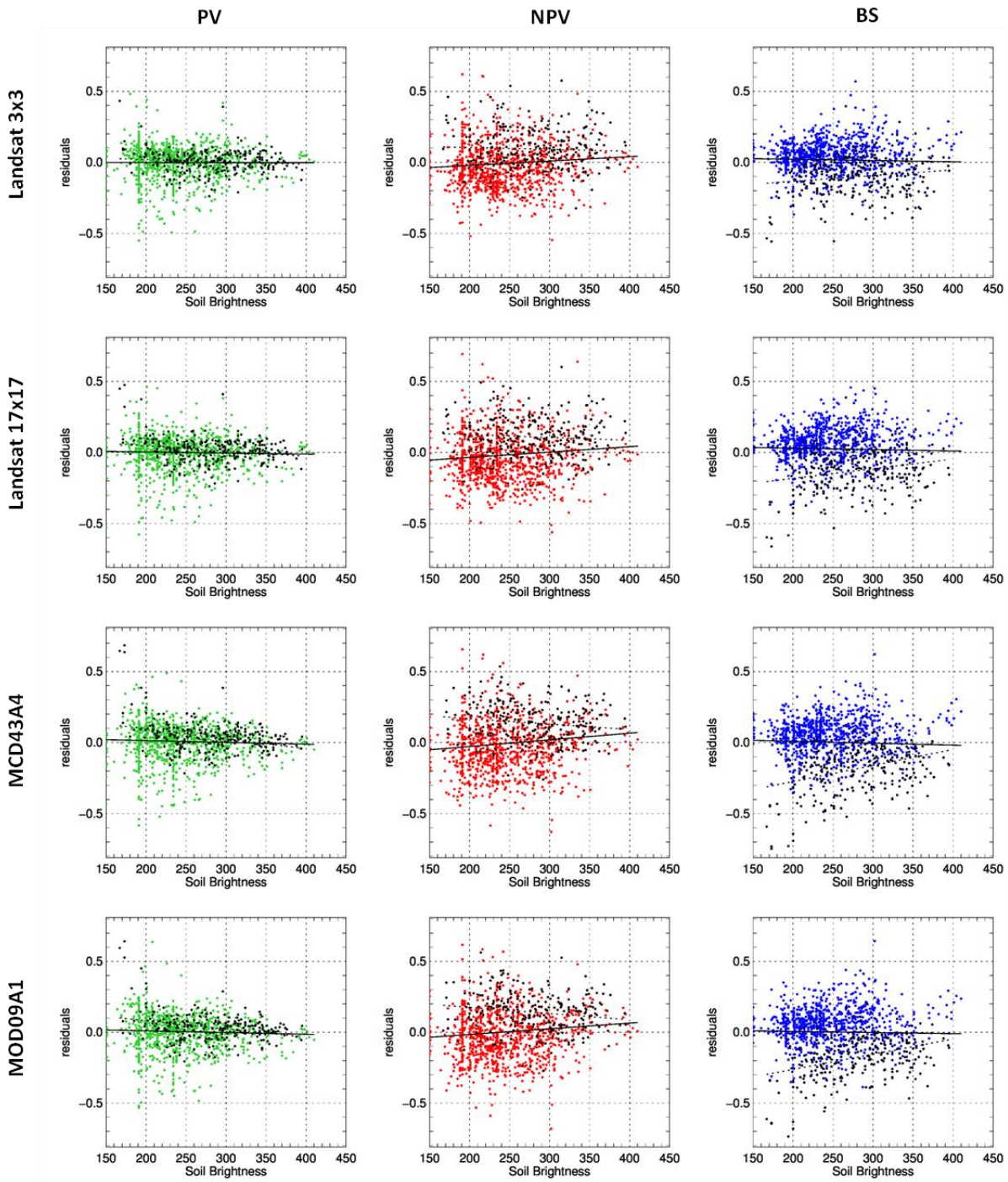


**Figure S3: Scatterplots of the model residuals (estimated-observed) and the soil brightness as derived from the sum of the red, green and blue components. Landsat 3x3 (top row), Landsat 17x17 (second row), MCD43A4 (third row) and MOD09A1 (bottom row). The black dots correspond to the observations with BS > 50%. The red and black lines show the linear fit to all points and to the black points respectively. Full statistics for these regressions are provided in Table 2.**

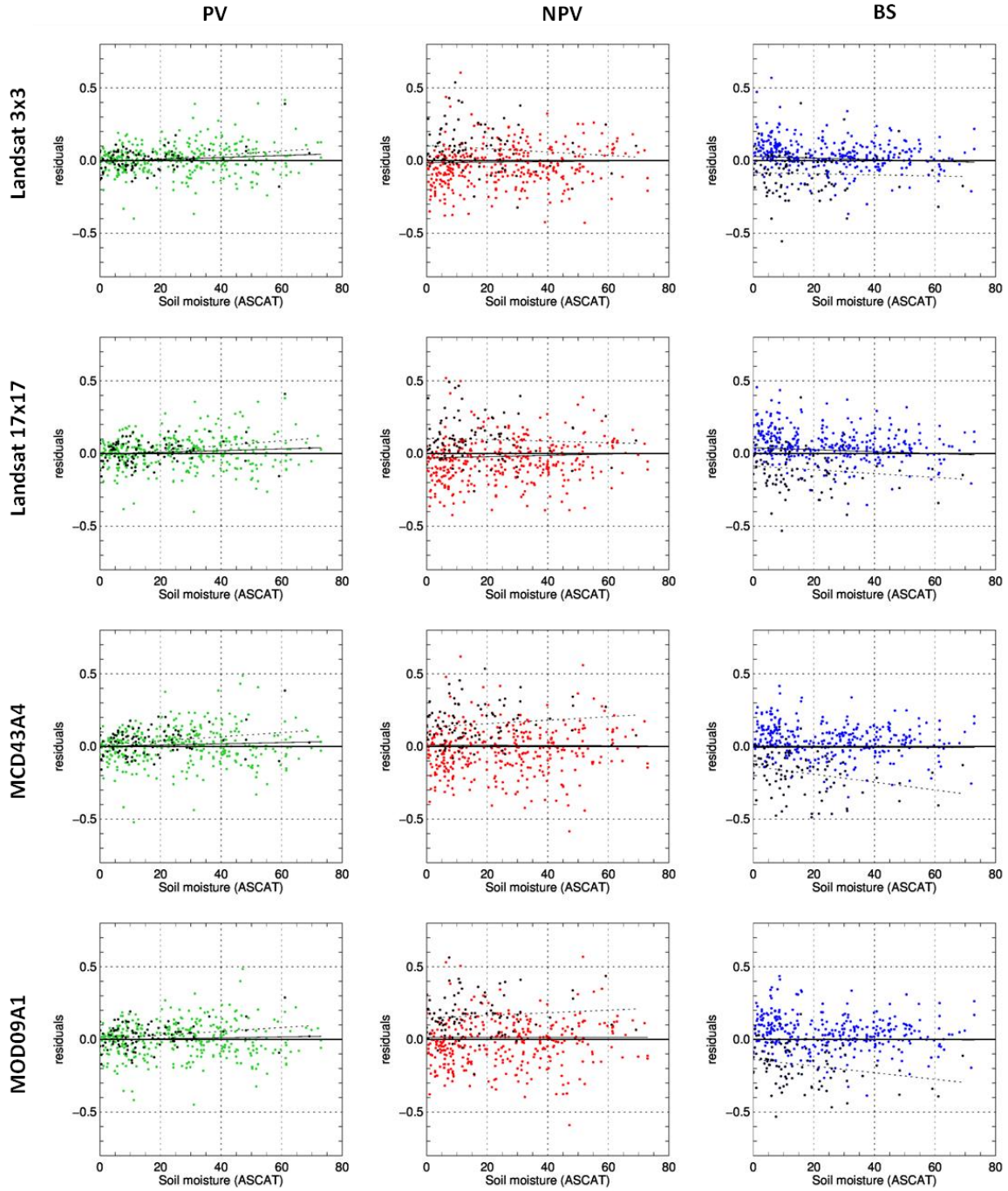


**Figure S4: Scatterplots of the model residuals (estimated-observed) and the soil moisture as derived from the ASCAT soil moisture product. Landsat 3x3 (top row), Landsat 17x17 (second row), MCD43A4 (third row) and MOD09A1 (bottom row). The black dots correspond to the observations with BS> 50%. The red and black lines show the linear fit to all points and to the black points respectively. Full statistics for these regressions are provided in Table 2.**

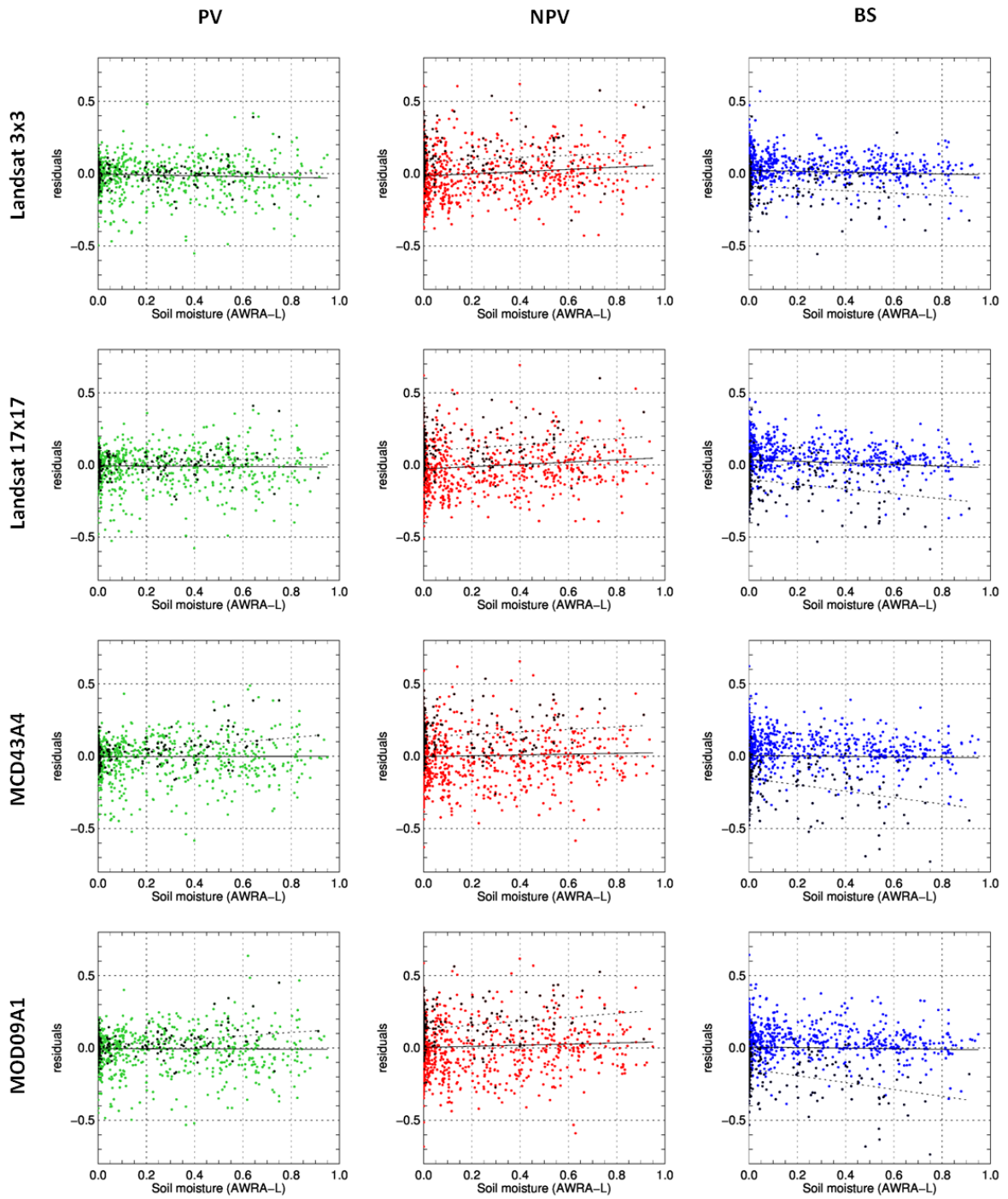


**Figure S5: Scatterplots of the model residuals (estimated-observed) and the soil moisture as derived from the AWRA-L v3.0 model. Landsat 3x3 (top row), Landsat 17x17 (second row), MCD43A4 (third row) and MOD09A1 (bottom row). The black dots correspond to the observations with  $BS > 50\%$ . The red and black lines show the linear fit to all points and to the black points respectively. Full statistics for these regressions are provided in Table 2.**

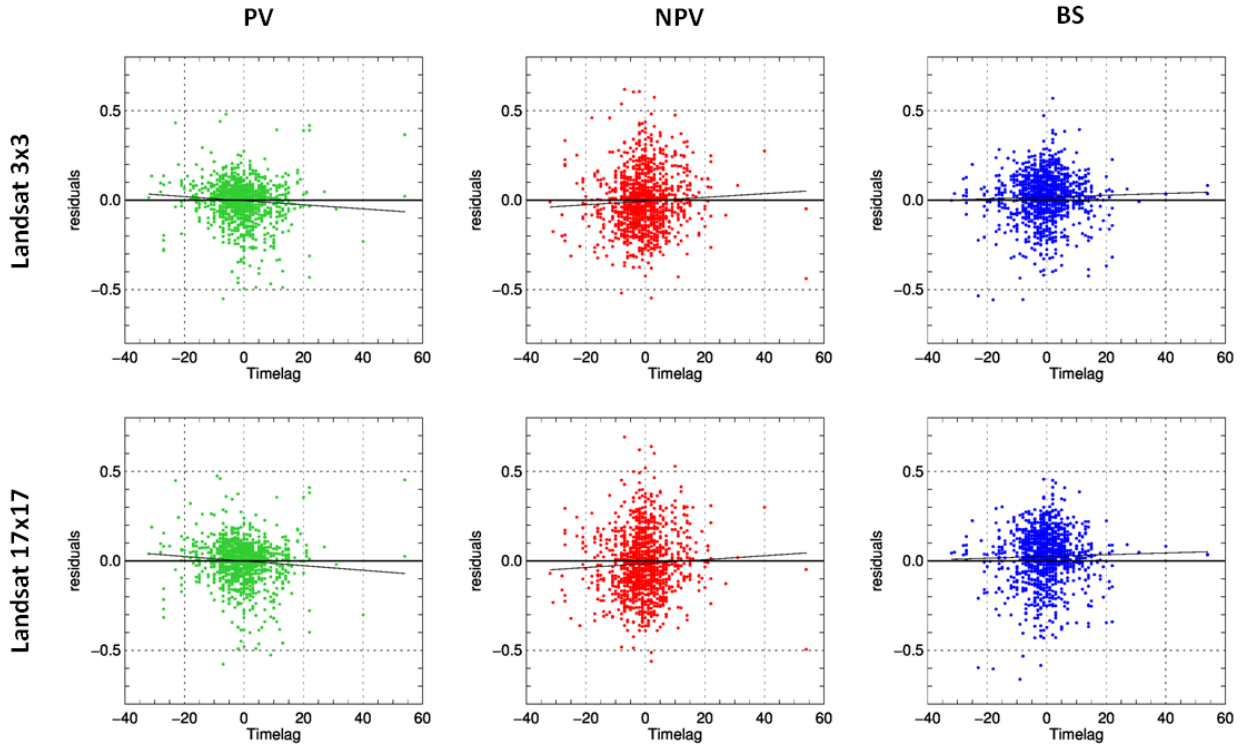


**Figure S6: Scatterplots of the model residuals (estimated-observed) and the timelag (days) between the date of the Landsat acquisition and the field observation. Negative numbers indicate that the Landsat image was previous to the field observation. The red line shows the linear fit to the points.**

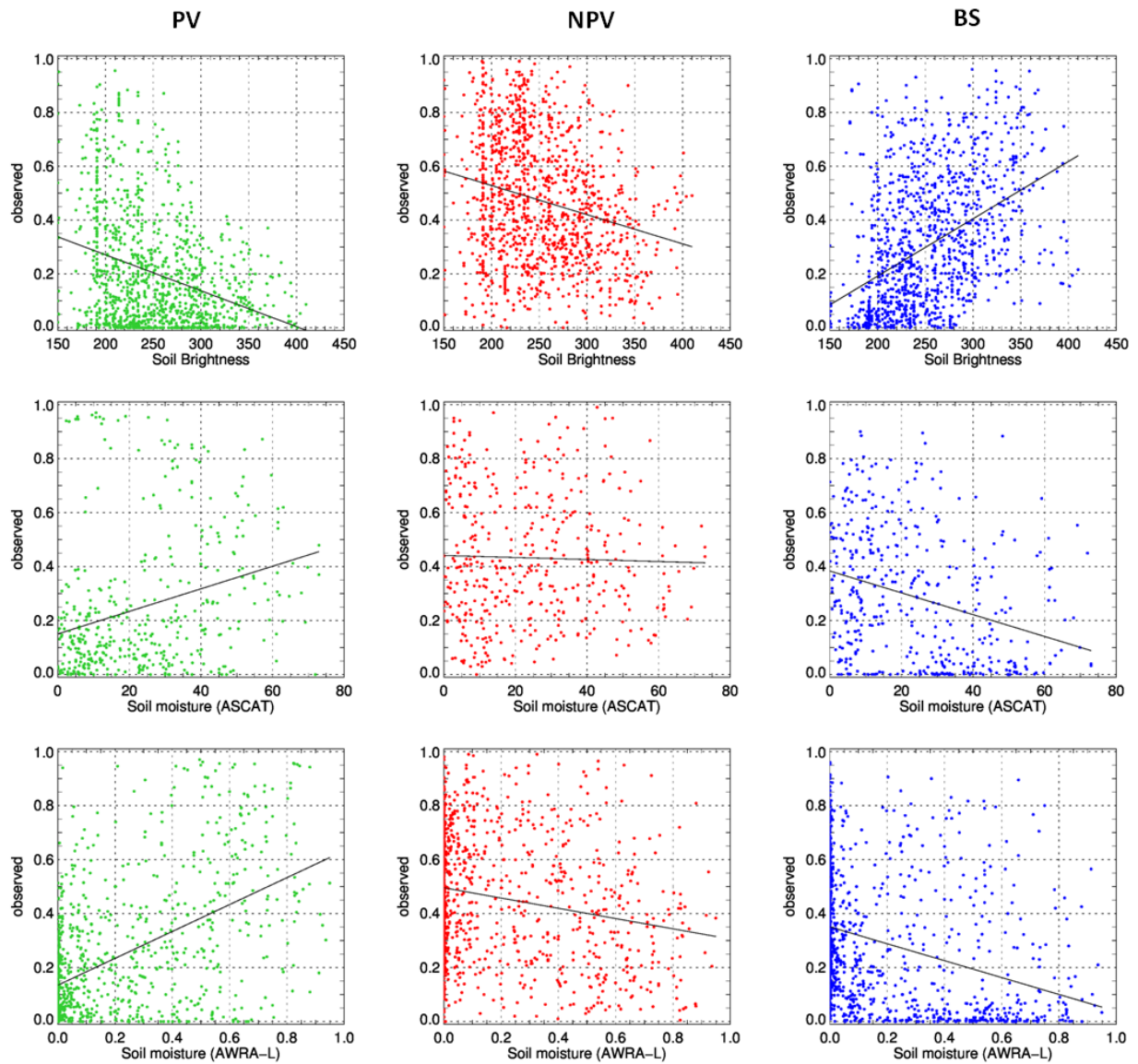


**Figure S7: Scatterplots of the field observations and the soil brightness and moisture as derived from the ASCAT soil moisture product and from the AWRA-L v3.0 model. The red line shows the linear fit to the data.**